

AN EXTENDED *FUSE* SURVEY OF DIFFUSE O VI EMISSION IN THE INTERSTELLAR MEDIUM¹

W. VAN DYKE DIXON AND RAVI SANKRIT

The Johns Hopkins University, Department of Physics and Astronomy, 3400 North Charles Street, Baltimore, MD 21218

AND

BIRGIT OTTE

University of Michigan, Astronomy Department, 500 Church Street, Ann Arbor, MI 48109

To appear in The Astrophysical Journal, Vol. 647, 10 August 2006

ABSTRACT

We present a survey of diffuse O VI emission in the interstellar medium obtained with the *Far Ultraviolet Spectroscopic Explorer (FUSE)*. Spanning 5.5 years of *FUSE* observations, from launch through 2004 December, our data set consists of 2925 exposures along 183 sight lines, including all of those with previously-published O VI detections. The data were processed using an implementation of CalFUSE v3.1 modified to optimize the signal-to-noise ratio and velocity scale of spectra from an aperture-filling source. Of our 183 sight lines, 73 show O VI $\lambda 1032$ emission, 29 at $> 3\sigma$ significance. Six of the 3σ features have velocities $|v_{\text{LSR}}| > 120 \text{ km s}^{-1}$, while the others have $|v_{\text{LSR}}| < 50 \text{ km s}^{-1}$. Measured intensities range from 1800 to 9100 LU, with a median of 3300 LU. Combining our results with published O VI absorption data, we find that an O VI-bearing interface in the local ISM yields an electron density $n_e = 0.2\text{--}0.3 \text{ cm}^{-3}$ and a path length of 0.1 pc, while O VI-emitting regions associated with high-velocity clouds in the Galactic halo have densities an order of magnitude lower and path lengths two orders of magnitude longer. Though the O VI intensities along these sight lines are similar, the emission is produced by gas with very different properties.

Subject headings: ISM: general — ISM: structure — Galaxy: structure — ultraviolet: ISM

1. INTRODUCTION

For gas in collisional ionization equilibrium, emission via the 1031.93 and 1037.62 Å resonance lines of the lithium-like O VI ion is the dominant cooling mechanism at temperatures of $(1\text{--}5) \times 10^5 \text{ K}$ (Sutherland & Dopita 1993). Gas cools rapidly at these temperatures, so O VI in the interstellar medium (ISM) traces regions in transition: hot gas cooling through temperatures of a few times 10^5 K or interfaces between cool or warm gas ($T = 10^2\text{--}10^4 \text{ K}$) and hot gas ($T = 10^6 \text{ K}$) where 10^5 K gas can form (Savage 1995).

Absorption-line studies have begun to reveal the distribution of O VI-bearing gas in the Galaxy. (For an excellent review, see Savage & Lehner 2006.) O VI absorption is detected in the spectra of UV-bright stars, QSOs, and AGNs (e.g., Wakker et al. 2003). Measurements along sight lines through the Galactic halo indicate that the O VI-bearing gas is roughly co-spatial with the thick disk, having a scale height of about 2.3 kpc (Savage et al. 2003). Within the thick disk, the distribution of O VI is patchy and varies on small angular scales ($0^\circ 05' \text{--} 5^\circ 0'$ toward the Magellanic Clouds; Howk et al. 2002). Measurements towards stars in the disk indicate that the O VI-bearing gas is extremely clumpy and cannot exist in uniform clouds (Bowen et al. 2006). These observations are consistent with the O VI being formed in interfaces (Savage & Lehner 2006).

Emission-line studies provide additional insight into the properties of transition-temperature gas. While absorption-line studies reveal the velocity distribution of

O VI-bearing gas along a line of sight, they are limited to sight lines with bright background sources. Emission-line observations can probe (and eventually map) the entire sky, but with lower spectral and spatial resolution. Particularly useful are measurements of O VI absorption and emission along a single line of sight. The absorption is proportional to the density of the gas, while the emission is proportional to the square of the density. If the same gas is responsible for both absorption and emission, these measurements can be combined to derive the electron density in the plasma (Shull & Slavin 1994). Assuming a gas temperature and oxygen abundance, one can derive the O VI density and path length through the emitting gas.

Until recently, convincing detections of O VI emission from the diffuse interstellar medium were limited to fewer than a dozen sight lines probed with the *Far Ultraviolet Spectroscopic Explorer (FUSE)* (Table 1). Reported intensities range from 1.6 to $3.3 \times 10^3 \text{ LU}$. (One photon $\text{cm}^{-2} \text{ s}^{-1} \text{ sr}^{-1}$ or line unit corresponds to $1.9 \times 10^{-11} \text{ erg cm}^{-2} \text{ s}^{-1} \text{ sr}^{-1}$ at 1032 Å.) Korpela et al. (2006) present a deep far-ultraviolet emission spectrum from a region of 15° radius centered on the north ecliptic pole obtained with the *Spectroscopy of Plasma Evolution from Astrophysical Radiation (SPEAR)* instrument. They report a combined O VI $\lambda\lambda 1032, 1038$ intensity of 5724 LU, slightly higher than the initial *FUSE* results. Using archival data from the first four years of the *FUSE* mission, Otte & Dixon (2006) find measurable O VI $\lambda 1032$ emission along 23 of 112 sight lines and conclude that their data are consistent with the picture derived from O VI absorption surveys: high-latitude sight lines probe O VI-emitting gas in a clumpy, thick disk, while low-latitude sight lines sample mixing layers and interfaces in the thin disk of the Galaxy. Unfortunately, the small size and low signal-to-

¹ Based on observations made with the NASA-CNES-CSA *Far Ultraviolet Spectroscopic Explorer*. *FUSE* is operated for NASA by the Johns Hopkins University under NASA contract NAS5-32985. Electronic address: wvd@pha.jhu.edu

TABLE 1
PUBLISHED *FUSE* O VI $\lambda 1032$ MEASUREMENTS AND UPPER LIMITS

Sight Line	l (deg.)	b (deg.)	I_{1032}^a (10^3 LU)	FWHM (km s $^{-1}$)	v_{LSR} (km s $^{-1}$)	Ref.
A11701	57.6	+88.0	2.0 ± 0.6	23 ± 55	-17 ± 9	1
S40548	95.4	+36.1	1.6 ± 0.3	75 ± 3	-50 ± 30	2
S40561	99.3	+43.3	≤ 1.6	2
P11003	113.0	+70.7	2.6 ± 0.4	75	10	3
B00303	156.3	+57.8	3.3 ± 1.1	210	-51 ± 30	4
B00302	162.7	+57.0	2.5 ± 0.7	150	-16 ± 22	4
B12901	278.6	-45.3	≤ 0.5	5
A11703	284.0	+74.5	2.9 ± 0.7	< 80	84 ± 15	1
I20509	315.0	-41.3	2.9 ± 0.3	160	64	6

REFERENCES. — (1) Dixon et al. 2001; (2) Otte et al. 2003; (3) Shelton 2002; (4) Welsh et al. 2002; (5) Shelton 2003; (6) Shelton et al. 2001

$^a 1 \text{ LU} = 1 \text{ photon s}^{-1} \text{ cm}^{-2} \text{ sr}^{-1}$.

noise (S/N) ratio of their sample (only 11 of their O VI features are 3σ detections) limit their ability to constrain the properties of the emitting gas.

To better constrain the physical properties of O VI-bearing gas in the ISM, we have conducted an extended *FUSE* survey of diffuse O VI emission in the interstellar medium, using all *FUSE* data obtained through 2004 December and the latest version of the CalFUSE calibration pipeline. The results are presented in this paper, which is organized as follows: In §2, we discuss the *FUSE* instrument and our selection of survey sight lines from the *FUSE* archive. In §3, we describe our data-reduction techniques, with emphasis on our modifications to the standard CalFUSE pipeline. §4 describes our method for identifying O VI emission features and measuring their parameters. We discuss our results in §5. In §6, we combine O VI emission and absorption data to derive the properties of O VI-bearing gas in the Galactic disk and thick disk/halo. Results are summarized in §7. An appendix discusses the origin of the emission seen toward sight lines P12011 and B12901. Unless otherwise noted, all wavelengths in this paper are heliocentric, and all velocities are quoted relative to the local standard of rest (LSR). We use the kinematical LSR, in which the standard solar motion is 20 km s^{-1} towards $\alpha = 18\text{h}$, $\delta = +30^\circ$ (1900).

2. OBSERVATIONS

The *FUSE* instrument consists of four independent optical paths. Two employ LiF optical coatings and are sensitive to wavelengths from 990 to 1187 Å, and two use SiC coatings, which provide reflectivity to the Lyman limit. The four channels overlap between 990 and 1070 Å. Each channel possesses three apertures that simultaneously sample different parts of the sky. The low-resolution (LWRS) aperture is $30'' \times 30''$ in size. The medium-resolution (MDRS) aperture spans $4'' \times 20''$ and lies about $3/5$ from the LWRS aperture. The high-resolution (HIRS) aperture lies midway between the MDRS and LWRS apertures and samples an area of $1''.25 \times 20''$. A fourth location, the reference point (RFPT), is offset from the HIRS aperture by $60''$. When a star is placed at the reference point, all three apertures sample the background sky. For a complete description of *FUSE*, see

Moos et al. (2000) and Sahnou et al. (2000).

The data sets used in our survey fall into three categories. First are the S405, S505, and Z907 programs. S405 and S505 represent background observations, some near *FUSE* targets (with the target at the RFPT), others with the LWRS aperture centered on the orbit pole. The Z907 program consists of extragalactic targets intended as background sources for absorption-line studies. When these targets are sufficiently faint, we include them in our sample. Second, we searched the Multimission Archive at Space Telescope (MAST) for MDRS and HIRS observations of point sources obtained in time-tag mode, as their LWRS apertures should sample only background radiation. Third, we include all *FUSE* sight lines with previously-published detections of diffuse O VI emission (Table 1).

We exclude from our sample all sight lines probing known supernova remnants or planetary nebulae, since these structures do not represent the diffuse interstellar medium. Sight lines that probe the Magellanic Clouds (Sankrit et al., in preparation), the Coalsack Nebula (Andersson et al. 2004), and the emission nebula around KPD 0005+5106 (Otte, Dixon, & Sankrit 2004) are presented elsewhere and are not included here. This sample is a superset of that presented by Otte & Dixon (2006), which includes only data obtained through 2003 July.

We use only data from the LiF 1A channel in our analysis. Because its sensitivity at 1032 Å is more than twice that of any other channel, including data from other channels would reduce the signal-to-noise ratio of the resulting spectrum. We use only data obtained in time-tag mode, which preserves arrival time and pulse-height information for each photon event. This is the default observing mode for faint targets. Previous observers (e.g., Shelton et al. 2001; Shelton 2002; Otte, Dixon, & Sankrit 2003) have detected faint (presumably geocoronal) emission on the blue wing of the O VI $\lambda 1032$ line in *FUSE* spectra obtained during orbital day, so we use only data obtained during orbital night. Individual exposures with less than 10 s of night exposure time are excluded from the survey, as are combined data sets with less than 1500 ks of total night exposure time or with significant continuum flux. Finally, we use only data obtained from launch (1999 June) through 2004 December.

Table 2 lists the 183 sight lines in our survey and the *FUSE* observations contributing to each. Each observation consists of many exposures; our sample contains 2925 exposures from 375 observations. Note that we combine data from multiple observations — and sometimes multiple science programs — that sample the same or nearby lines of sight. The orientation of the *FUSE* spacecraft is specified by four quantities: the right ascension and declination of the target, the aperture in which the target is centered, and the astronomical roll angle (east of north) of the spacecraft about the target (and thus the center of the target aperture). The roll angle is constrained by operational requirements and varies throughout the year. Because we combine data sets without regard to the original target aperture (HIRS, MDRS, LWRS, or RFPT) or roll angle, a sight line listed in Table 2 may represent data obtained from regions of the sky separated by up to 7 arcmin (twice the distance between the LWRS and MDRS apertures).

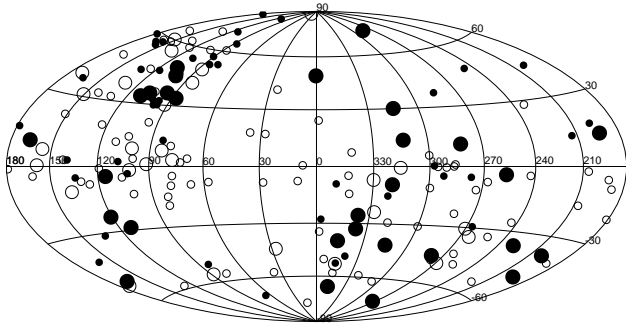


FIG. 1.— Distribution of survey sight lines on the sky. Large solid circles represent 3σ detections. Small solid circles represent 2σ detections. Large open circles represent non-detections with upper limits less than 2000 LU. Small open circles represent non-detections with higher upper limits. Galactic coordinates are used in a Hammer-Aitoff projection.

The distribution of survey sight lines on the sky is presented in Fig. 1. The survey sample of Otte & Dixon (2006) is concentrated in two quadrants, the northern sky with $0^\circ < l < 180^\circ$ and the southern sky with $180^\circ < l < 360^\circ$, due to observational constraints that reduced target availability in the orbit plane, which stretches across the Galactic center. Improvements in pointing control implemented later in the mission have partially filled in the other two quadrants, but the distribution remains skewed. Note especially the high concentration of targets in the region with $90^\circ < l < 180^\circ$ and $b > 30^\circ$. This 1/16 of the sky contains more than twice as many targets as any other region of equal area.

3. DATA REDUCTION

The data are reduced using an implementation of CalFUSE v3.1, the latest version of the *FUSE* data-reduction software package (Dixon et al., in preparation), optimized for a faint, diffuse source. Specifically, the pipeline is instructed to reject data obtained during orbital day. The first three modules of the pipeline (`cf_ttag_init`, `cf_convert_to_farf`, and `cf_screen_photons`) are run as usual, then the file-header keywords `SRC_TYPE` and `APERTURE` are set to `EE` and `LWRS` (to indicate an extended, emission-line source in the low-resolution aperture), respectively. Prematurely modifying these keywords confuses the screening routines, which can misinterpret a star drifting into the HIRS or MDRS aperture as a detector burst. The rest of the pipeline is run as usual, but with background subtraction turned off. Note that CalFUSE does not perform jitter correction, astigmatism correction, or optimal extraction on extended sources.

Apart from the above exceptions, we accept all of the default parameters defined by the pipeline. In particular, we accept all photon events with pulse heights in the range 2–25. To minimize the detector background, previous observers have imposed tighter pulse-height constraints, but we find that, because the mean pulse height of real photon events varies with time, reducing the range of allowed pulse heights can result in the rejection of real photon events for some time periods. We also accept the default spectral binning of 0.013 \AA , or approximately two detector pixels. The pipeline operates on one exposure

at a time, producing a flux- and wavelength-calibrated spectrum from each. Error bars are computed assuming Gaussian (\sqrt{N}) statistics.

The *FUSE* wavelength scale is nominally heliocentric, but nonlinearities in early versions of the CalFUSE wavelength solution forced previous observers to derive their wavelength scales from measurements of nearby O I airglow lines. The wavelength solution employed by CalFUSE v3.1 is far more accurate, but uncertainties in its zero point must be corrected by hand. We fit a synthetic emission feature (described below) to the Lyman β airglow line of each extracted spectrum and compute the shift in pixels necessary to place the line at zero velocity in a geocentric reference frame. (Actually, we shift the Lyman β line to $v_{\text{geo}} = +0.5 \text{ km s}^{-1}$, which places the O I $\lambda 1027$ line at rest. The fainter O I line is presumed to be less subject to detector effects that might skew its measured centroid.) Zero-point wavelength shifts are not random, but exhibit a periodicity on timescales of several hours. We take advantage of this fact for spectra with weak Lyman β features: if the line contains fewer than 200 raw counts, we do not attempt a fit, but interpolate a shift from the values computed for the other exposures. The spectra are combined using the program `cf_combine`, which shifts and sums the individual extracted spectral files.

4. MEASUREMENTS

4.1. Emission Line Profile

Shelton et al. (2001) adopt the observed profile of the O I $\lambda 1039$ airglow feature as the shape of an aperture-filling diffuse emission feature. We prefer to use a synthetic line profile, so fit this feature with a model emission line consisting of a top-hat function convolved with a Gaussian. The widths of both components are free parameters in the fit, as are the line intensity and centroid. Fits to 131 spectra with at least 500 counts in the line yield a best-fit width of $106.1 \pm 3.4 \text{ km s}^{-1}$ for the top hat and a $\text{FWHM} = 25.4 \pm 5.4 \text{ km s}^{-1}$ for the Gaussian (where the error bars represent the standard deviation about the mean). Fits to the O I $\lambda 1027$ airglow line yield similar results. The top hat represents the projection of the LWRS aperture onto the detector, while the Gaussian represents the finite resolution of the instrument. For point sources, the *FUSE* resolution is between 15 and 20 km s^{-1} , so a value of 25 km s^{-1} for a diffuse source is reasonable. Note that 106 km s^{-1} corresponds to 28 spectral pixels.

Several previous observers have followed Dixon et al. (2001) in adopting an unconvolved top hat for the shape of a diffuse emission feature, convolving it with a Gaussian to match the observed O VI line profile, and reporting the FWHM of the Gaussian as the intrinsic width of the emission feature. By ignoring the instrumental contribution to the smoothing of the top-hat function, this technique over-estimates the intrinsic width of the emission profile. Fortunately, the error is small: 10% for a best-fit FWHM of 50 km s^{-1} , 1% for 150 km s^{-1} .

To construct our model line profiles, we convolve the 106 km s^{-1} top-hat function with a single Gaussian, representing the combined effects of the intrinsic emission profile and the instrumental line-spread function. To optimize the model resolution, we employ a grid of 0.013

Å pixels and, rather than binning the model to match the data, smooth it by convolving with a second top-hat function either 8 or 14 pixels wide. Each curve is normalized so that the best-fit scale factor reported by our fitting routine equals the line intensity in LU. We generate a series of curves with Gaussian FWHM values from 1 to 1000 km s⁻¹.

4.2. Detection of O VI Emission

Following Martin & Bowyer (1990), we use an automated routine to search each composite spectrum for a statistically-significant emission feature near 1032 Å. The calculation is performed using the WEIGHTS array, which is effectively raw counts for low count-rate data. (Dixon et al., in preparation, discuss the format of *FUSE* calibrated spectral files.) The mean value of the WEIGHTS array in the regions 1029–1030 and 1033.5–1036 Å is adopted as the local continuum. At each pixel between 1030 and 1034 Å, we bin the data by the width of an emission feature and determine the counts in excess of the mean. The significance of this excess is computed assuming Gaussian statistics. We repeat this process for bin widths from 25 to 30 pixels, or ~ 94 to 113 km s⁻¹. From all combinations of central wavelength and line width, we select the most significant feature. If its significance is greater than 3σ , we record it as a detection. Table 3 lists our detection sight lines, Table 4 our non-detection sight lines. Our algorithm is designed to detect emission features that are ~ 106 km s⁻¹ in width; given our S/N, much narrower features are likely to be noise spikes, while much broader features are difficult to distinguish from the background.

Further analysis is performed on the flux-calibrated spectra, which are first binned to improve their signal-to-noise ratio. If the local continuum level (computed above) is greater than 1.5 raw counts per 0.013 Å pixel, we bin the spectrum by 8 pixels or 0.104 Å. A diffuse emission feature is about 3.5 binned pixels wide. If the continuum level is less than 1.5, we bin by 14 pixels or 0.182 Å, a value chosen so that a diffuse emission feature is spanned by 2 binned pixels. Most of our emission features are broad enough that 14-pixel binning provides sufficient spectral resolution; however, we find that emission features whose Gaussian components have FWHM values less than 100 km s⁻¹ can be undersampled at this resolution, so we lower the threshold for 8-pixel binning to 0.5 raw counts per 0.013 Å pixel for spectra containing these narrow features. The binning applied to each of our spectra is listed in Table 3. After binning, the FLUX and ERROR arrays are converted from units of erg cm⁻² s⁻¹ Å⁻¹ to LU pixel⁻¹, and the ERROR array is smoothed by 5 pixels, which removes zero-valued error bars without significantly changing its shape.

To derive the line parameters of each emission feature, we fit model spectra to the flux-calibrated data using the nonlinear curve-fitting program SPECFIT (Kriss 1994), which runs in the IRAF² environment, to perform a χ^2 minimization of the model parameters. Our synthetic

line profiles are described above. The program interpolates between tabulated curves to reproduce the shape of the emission line. Free parameters in the fit are the level and slope of the continuum (assumed linear) and the intensity, wavelength, and Gaussian FWHM of the model line. For most sight lines, we model only the region 1028.7–1036.5 Å. We do not attempt to fit the O VI 1038 Å feature, as it is only half as strong as the 1032 Å line in an optically-thin gas and is often blended with emission from interstellar C II* λ 1037.02.

Best-fit values for the O VI λ 1032 line parameters are reported in Table 3, and plots of the spectra and best-fit models are presented in Figures 2 and 3. In the table and figures, as throughout this paper, we distinguish between 3σ detections, for which $I/\sigma(I) \geq 3$, and 2σ detections, for which $I/\sigma(I) < 3$. All of these features meet our requirement of having an intensity greater than three times the uncertainty in the local continuum and are thus statistically significant; however, to derive the physical properties of the O VI-bearing gas, we consider only those features whose intensities are certain at the 3σ level.

The FWHM values in Table 3 include the smoothing imparted by the instrument optics; values less than ~ 25 km s⁻¹ indicate that the emission does not fill the LWRs aperture. In such cases, the surface brightness of the emitting region will be underestimated, because the conversion to LU assumes that the emission fills the aperture, and the velocity of the emitting gas will be uncertain, because it may not be centered in the aperture.

The quoted uncertainties are the error bars returned by SPECFIT, which are obtained from the error matrix and correspond to a 1σ confidence interval for a single interesting parameter. For multi-parameter fits with more than one interesting parameter, this method can underestimate the true uncertainty in each, so we have computed more rigorous error bars for sight line I20509 (for which the S/N is high and the O VI λ 1032 line is broad) in the following way: For each model parameter, we begin with the best-fit value, then increase it, while re-optimizing the other model parameters, until χ^2 increases by 1.0 (Press et al. 1988). We find that the two methods yield identical error bars, suggesting that the SPECFIT errors are sufficient for well-sampled spectra.

Both the *FUSE* flux calibration, which is based on theoretical models of white-dwarf stellar atmospheres, and the solid angle of the LWRs aperture are known to within about 10% (Sahnou et al. 2000). Added in quadrature, they contribute a systematic uncertainty of $\sim 14\%$ (Shelton et al. 2001) in addition to the statistical uncertainties quoted in Table 3.

Our best-fit line intensities are lower limits, in the sense that the intrinsic O VI intensity may be higher than is observed. We discuss the effects of dust extinction in §5.1. Resonance scattering within the O VI-bearing gas can also have a strong effect on the observed intensity. For an optically thin gas, the intensity ratio $I_{1032}/I_{1038} = 2$, whereas an optically thick plasma yields a ratio of unity. Since the O VI λ 1038 line is generally difficult to measure (as mentioned above) and its intensity has a large uncertainty, the resulting line ratio is usually inconclusive. We therefore do not attempt to estimate the self absorption along our detection sight lines.

Because molecular hydrogen is ubiquitous in the ISM,

² The Image Reduction and Analysis Facility (IRAF) is distributed by the National Optical Astronomy Observatories, which is supported by the Association of Universities for Research in Astronomy (AURA), Inc., under cooperative agreement with the National Science Foundation.

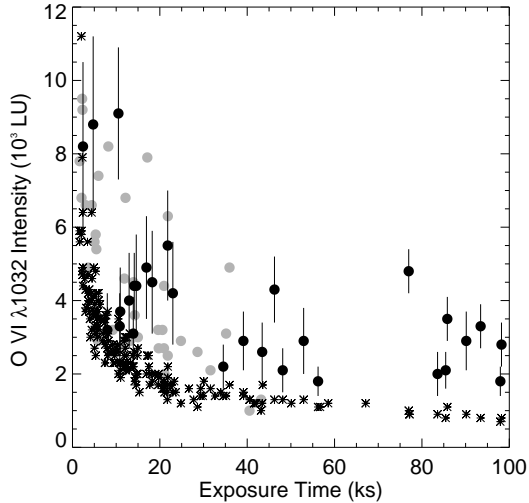


FIG. 4.— Observed O VI $\lambda 1032$ intensities and upper limits. Black circles represent 3σ detections. Grey circles (without error bars) represent 2σ detections. Asterisks represent the 3σ upper limits computed for all sight lines as described in the text. *FUSE* can detect O VI emission as faint as 2000 LU in 18 ks and as faint as 1000 LU in 80 ks (night only).

we must consider the effects of H_2 absorption and emission on our results. The H_2 features nearest O VI $\lambda 1032$ are the Lyman (6,0) $P(3)$ and $R(4)$ lines at 1031.19 and 1032.36 Å, respectively, but these features are weak in cold (~ 100 K), diffuse clouds (Shull et al. 2000) and will not significantly reduce the observed intensity of the O VI $\lambda 1032$ feature. Another possibility is that fluorescent H_2 contributes to the observed O VI emission. Following Shelton et al. (2001), we search for the Werner (0,1) $P(3)$ $\lambda 1058.82$ line, which for cool clouds bathed in ultraviolet light should be at least 50% brighter than any of the H_2 emission lines between 1030 and 1040 Å (Sternberg 1989), but none of our 3σ sight lines exhibits a statistically significant emission feature near 1059 Å.

4.3. Upper Limits on O VI Emission

For non-detection sight lines, we compute 3σ upper limits to the intensity of an O VI emission feature using the mean value of the FLUX array between 1030 and 1035 Å and assuming a line width of 28 pixels (106 km s $^{-1}$). The resulting limits are given in Table 4. To obtain more data points with long integration times, we repeat the exercise using our detection sight lines, but masking out the O VI line when computing the continuum level. Figure 4 presents both sets of limits as a function of exposure time. *FUSE* can detect diffuse O VI emission as faint as 2000 LU in 18 ks of night exposure time and as faint as 1000 LU in ~ 80 ks of night time.

4.4. Comparison with Previously-Published Sight Lines

It is instructive to compare our results with the previously-published values listed in Table 1. Four of the published sight lines, A11701, B00303, B00302, and P11003, fail one or more of our statistical filters. A11701 yields only an upper limit on the O VI intensity, while the other three produce 2σ detections. In three of these four cases, the original analysis used both day and night

data, which explains our lower S/N ratios. Similarly, CalFUSE rejects most of the night exposure time for sight line S40561 due to limb-angle violations, raising our upper limit on the O VI intensity. For sight line S40548, we obtain the published line intensity if we fix the Gaussian line width to be 75 km s $^{-1}$, but find the best-fit intensity and Gaussian FWHM to be a factor of two larger. Sight line B12901 is discussed in § A.2. The remaining sight lines, A11703 and I20509, yield 3σ detections in our survey. In both cases, our intensities and derived FWHM values agree (within the errors) with the previously-published values. In neither case do our LSR velocities agree, illustrating the difficulty of deriving an accurate wavelength scale from nearby airglow features, as previous authors were required to do.

The results of Otte & Dixon (2006) are not included in Table 1. Comparison with their results is complicated by the fact that several of their sight lines appear in our survey with additional exposure time or combined with nearby lines of sight. Even so, when they report a 3σ detection, their best-fit line parameters generally agree with ours within the quoted errors. The recent *SPEAR* results are discussed in § 5.2.

5. RESULTS

Measured O VI $\lambda 1032$ intensities and upper limits for our survey sight lines are presented in Fig. 4. O VI emission is detected at 3σ significance along 29 lines of sight. Measured intensities range from 1800 to 9100 LU, with a median of 3300 LU, an average of 3900 LU, and a standard deviation 1900 LU. An additional 44 sight lines exhibit O VI $\lambda 1032$ emission at lower significance, while 110 non-detection sight lines provide 3σ upper limits on the O VI intensity, 35 of them less than 2000 LU. The median value of all the 3σ limits is 2600 LU. The upper limits are strongly correlated with exposure time and generally lower than the measured intensities along detection sight lines with comparable exposure time. For our complete sample, the O VI detection rate (at 3σ significance) is 16%. If we consider only sight lines with exposure times greater than 18 ks (for which 3σ upper limits are less than 2000 LU), the detection rate rises to 30%.

5.1. Dust Extinction

UV emission is strongly attenuated by interstellar extinction. A color excess $E(B - V)$ of 0.05 magnitudes reduces the flux at 1032 Å by a factor of 2, and a color excess of 0.18 magnitudes by a factor of 10 (Fitzpatrick 1999). Thus, when we detect O VI emission in a direction with high extinction, we assume that the emission arises in the local ISM, i.e., closer than the dust causing most of the extinction. On the other hand, emission detected in directions of low extinction does not necessarily arise in the distant ISM, but may come from relatively nearby gas. Figure 5 presents a plot of color excess versus $\sin |b|$, where b is the Galactic latitude, for each sight line in our survey. We see that extinction falls rapidly as one moves away from the Galactic plane. We caution that interstellar extinction is variable on small spatial scales, and the Schlegel, Finkbeiner, & Davis (1998) values presented in Fig. 5 are based on *IRAS* maps with low spatial resolution. An example of an O VI detection through a region of patchy extinction is discussed in § A.2.

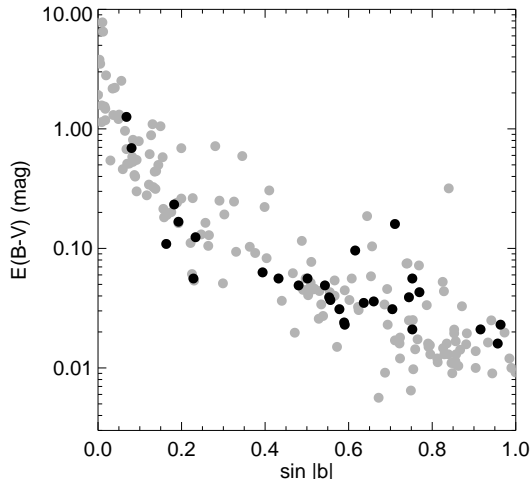


FIG. 5.— Variation of color excess with Galactic latitude. Black circles represent sight lines with 3σ detections. Grey circles represent the rest of our sample. Data are from Schlegel et al. 1998.

5.2. O VI Emission-Line Intensities

In Fig. 6, we plot O VI intensity against $\sin |b|$, where b is the Galactic latitude of the observed sight line. The emission features plotted as open circles have absolute velocities greater than 120 km s^{-1} . We discuss these sight lines and their possible relationship with high-velocity clouds (HVCs) in § 5.3. Of the 23 low-velocity sight lines, two have O VI intensities greater than 8000 LU, while the others range from 1800 to 5500 LU. Both high-intensity sight lines probe regions known to be energized by hot stars and supernova remnants. P12011 (discussed in § A.1) intersects the Monogem Ring, which is about 800 pc away, and S50508 probes the outskirts of the Vela supernova remnant (250 pc distant) and the Gum Nebula, which probably lies somewhat beyond Vela.

Based on observations with *SPEAR*, Korpela et al. (2006) report a combined O VI $\lambda\lambda 1032, 1038$ intensity of 5724 ± 570 (statistical) ± 1100 (systematic) LU for the region of 15° radius centered on the north ecliptic pole ($l = 123$, $b = +29^\circ$). The grey cross in Fig. 6 represents the *SPEAR* sight line. Its intensity is consistent with the *FUSE* data points in this latitude range. Two of our 3σ detections and one of our strong upper limits lie within the region sampled by *SPEAR*: P10429 ($I(1032) = 2900 \pm 800$ LU), Z90715 ($I(1032) = 4400 \pm 1400$ LU), and D11701 ($I(1032) < 1400$ LU).

Restricting our attention to the low-velocity, low-intensity O VI measurements plotted in Fig. 6, we note that the sight lines at high latitude tend to be fainter than average. The median intensity for this sample of 21 detections is 3500 LU, with a 95% confidence interval of (2700, 4500) LU. The median intensity for sight lines with $\sin |b| < 0.7$ is 4100 LU with confidence interval (3100, 4400) LU. For sight lines with $\sin |b| > 0.7$, these values are 2200 LU, (1800, 3700) LU. The median estimates for the two groups are quite different, but the 95% confidence intervals overlap. The overlap is driven by a single high-latitude point (A11703, at 3700 LU), which determines the upper limit of the confidence interval for its group. Although the equality of medians cannot be

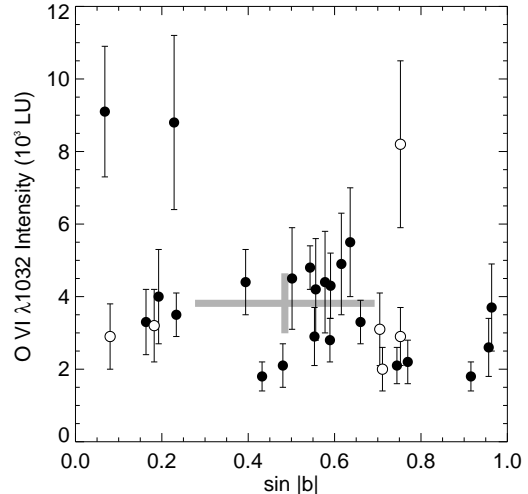


FIG. 6.— Variation of observed O VI $\lambda 1032$ intensity with Galactic latitude. Only 3σ detections are shown; open circles represent those with $|v_{\text{LSR}}| > 120 \text{ km s}^{-1}$. The grey cross represents the *SPEAR* observation of the 15° -radius region centered on the north ecliptic pole ($l = 123$, $b = +29^\circ$) reported by Korpela et al. 2006.

statistically excluded (at the 95% level), the data suggest that O VI emission tends to be fainter at high than at low latitudes.

A variation in the O VI intensity with latitude might result from either of two competing effects: First, interstellar extinction falls steeply as one moves off the Galactic plane (Fig. 5), so attenuation is lower at high latitudes. Second, the path length through the Galactic disk scales inversely with $\sin |b|$, so high-latitude sight lines may intersect fewer O VI-bearing regions. We have calculated the relative importance of these effects for a uniform distribution of O VI-bearing clouds in the disk, assuming that the extinction is local. At low latitudes ($\sin |b| < 0.1$), attenuation dominates completely, and the observed emission must come from nearby regions. Intensities rise gradually for $0.1 < \sin |b| < 0.4$, as the extinction decreases faster than the path length. At high latitudes, the two effects nearly cancel, and intensities are roughly constant for $\sin |b| > 0.4$. Models assuming an exponential distribution of the O VI-bearing clouds yield similar results. Thus, the low O VI intensities seen along sight lines with $\sin |b| > 0.7$ in Fig. 6 cannot be explained only by differences in path length. We suggest that the O VI-emitting regions at high latitudes are intrinsically fainter than those at low latitudes. The faint regions likely constitute a population in the thick disk or halo (perhaps with properties similar to those of the HVCs located in the same region of Fig. 6), while the brighter regions lie in the disk of the Galaxy. It is possible that the O VI detected along mid-latitude sight lines includes both disk and thick-disk emission, but for the lowest-latitude sight lines, the emitting regions necessarily lie in the disk.

5.3. O VI Emission-Line Velocities

The six 3σ detections plotted as open circles in Fig. 6 have absolute velocities greater than 120 km s^{-1} , corresponding to the velocities of HVCs. O VI absorp-

tion associated with H I high-velocity clouds was first detected by Sembach et al. (2000) and Murphy et al. (2000). Savage et al. (2003) report that, when a known H I HVC is present along a line of sight to an object, high-velocity O VI absorption spanning the approximate velocity range of the H I HVC is usually seen. The association of O VI with HVCs suggests that the O VI may be produced at interfaces between the H I clouds and hot, low-density gas in the Galactic corona or Local Group.

Two of our high-velocity sight lines, B12901 and S40549, intersect known H I HVCs and share the clouds' velocities. B12901 intersects the Magellanic Stream, while S40549 probes the HVC known as Complex C (see Fig. 16 of Wakker et al. 2003 and Figs. 11 and 13 of Sembach et al. 2003). These sight lines are discussed in §6.2. Sight line S40543, which is near S40549 on the sky, also intersects Complex C. The emission in S40543 has a high positive velocity, while Complex C has a high negative velocity; however, high-positive-velocity O VI absorption is seen nearby (Sembach et al. 2003). Sight lines C06401 and S30402 do not intersect HVCs. P10414 and S30402 probe low-latitude sight lines with high extinction, so their emission probably originates in the nearby disk (but see the discussion of patchy extinction in § A.2). Perhaps they sample fast-moving gas in previously undetected supernova remnants. (Note that the H α intensity along S30402 is unusually high.)

In Fig. 7, the LSR velocities of our low-velocity 3σ emission features are plotted against $\sin|b|$. The grey bars represent the range of LSR velocities predicted for each sight line by a simple model of Galactic rotation. Assuming a differentially-rotating halo with a constant velocity of $v = 220 \text{ km s}^{-1}$, we compute the expected radial velocity as a function of distance for the first 5 kpc along each line of sight. The model ignores broadening due to turbulence or any other motion. The three sight lines with $\sin|b| > 0.5$ and $v_{\text{LSR}} < -40 \text{ km s}^{-1}$ may probe intermediate-velocity clouds. The velocities of the remaining sight lines are generally consistent with Galactic rotation.

5.4. O VI Emission-Line Widths

Seven of our 3σ sight lines have best-fit Gaussian FWHM values less than 25 km s^{-1} , which indicates that their O VI-emitting regions do not fill the $30'' \times 30''$ LWRs aperture. Of the seven, C07601 and S50504 include data from lines of sight separated by an arc minute or more. The other five each sample a single line of sight. The data set with the longest exposure time, and thus the highest S/N, is S50510. We fit its spectrum with a model similar to that used to parameterize the O I $\lambda 1039$ airglow line: a top-hat function convolved with a Gaussian. The width of the top hat, together with the line intensity and centroid, are free parameters in the fit, but the Gaussian FWHM is fixed at 15 km s^{-1} , the instrumental resolution for a point source. (If allowed to vary freely, the Gaussian FWHM falls below 1 km s^{-1} .) For numerical simplicity, we fit the raw-counts spectrum, first binning the data by four pixels, which raises the background to ~ 10 counts per binned pixel. The width of the best-fit top-hat function is $80 \pm 15 \text{ km s}^{-1}$, significantly less than the 106 km s^{-1} width of an aperture-filling emission feature. By simple scaling, we derive an angular size of about $23''$ for the emitting region. Its spa-

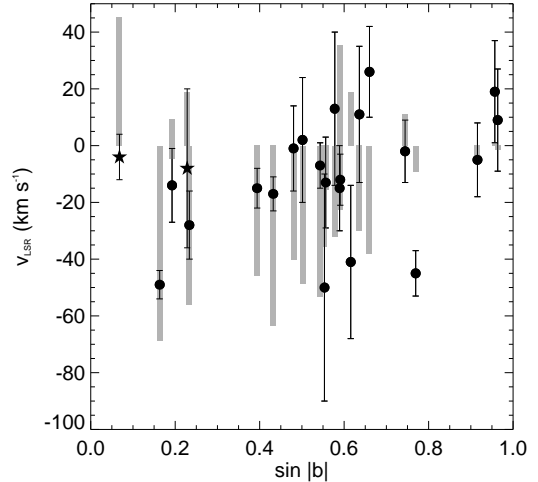


FIG. 7.— Variation of v_{LSR} with Galactic latitude. Only 3σ detections are shown. The two high-intensity sight lines discussed in §5.2 are plotted as stars. Sight lines with $|v_{\text{LSR}}| > 120 \text{ km s}^{-1}$ are not included. Grey bars represent the range of LSR velocities predicted for the first 5 kpc along each sight line by a simple model of Galactic rotation.

tial scale is distance dependent; at a distance of 1 kpc, $23''$ corresponds to about 0.1 pc.

5.5. Comparison with H α and Soft X-ray Emission

Perusal of the H α map produced by the Wisconsin H-Alpha Mapper (WHAM) Northern Sky Survey (Haffner et al. 2003) reveals that our O VI detection sight lines probe a variety of environments: toward H II regions, filaments, and bubbles, as well as toward faint, featureless, ionized gas. For each of our sight lines, Tables 3 and 4 list the H α intensities (integrated over one degree on the sky and over the velocity range $-80 \text{ km s}^{-1} < v < +80 \text{ km s}^{-1}$) measured by WHAM. We find no correlation between the O VI and H α intensities.

One possible origin of the observed O VI emission is hot gas cooling from temperatures of 10^6 K or more. Gas at these temperatures is observable in the soft X-ray (SXR) regime. Figure 8 presents the distribution of our 3σ detections and strong upper limits on a map of the $1/4 \text{ keV}$ X-ray sky observed with *ROSAT* (Snowden et al. 1997). Prominent features include the North Polar Spur, which arches from $(l, b) = (30, +30)$ to $(290, +60)$ and may be probed by sight line A11703 ($284, +75$); the Vela supernova remnant at $(260, -5)$, whose outer regions may be probed by sight line S50508 ($257, -4$); and the Monogem Ring, a supernova remnant centered near $(205, +15)$, which may be probed by sight line P12011 ($194, +13$). Tables 3 and 4 list the *ROSAT* $1/4 \text{ keV}$ SXR emission observed toward each of our sight lines. We find no correlation between the O VI and SXR intensities. In their O VI absorption-line survey, Savage et al. (2003) find no significant correlation between $N(\text{O VI})$ and either $I(\text{H}\alpha)$ or $I(\text{SXR})$.

6. PROPERTIES OF THE O VI-BEARING GAS

Measurements of O VI emission and absorption can be combined to provide valuable diagnostics of the O VI-bearing gas, so long as both probe the same interface or

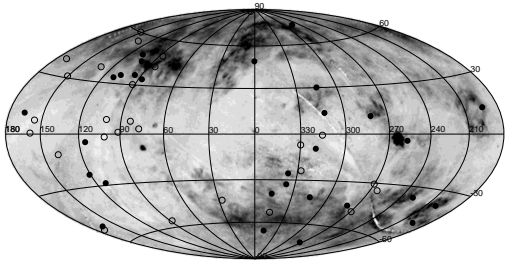


FIG. 8.— Distribution of survey sight lines on the SXR sky. Solid circles represent 3σ detections. Open circles represent non-detections with upper limits less than 2000 LU. The gray-scale map shows the 1/4 keV X-ray sky observed by *ROSAT* (Snowden et al. 1997). Galactic coordinates are used in a Hammer-Aitoff projection.

transition region. For a particular region, the intensity scales as $n_e^2 L$, where n_e is the electron density and L the path length through the region, while the column density scales as $n_e L$. From the ratio $I(\text{O VI})/N(\text{O VI})$, we can derive the electron density of the plasma (Shull & Slavin 1994) and, assuming an oxygen abundance, the path length through it. This calculation assumes that the density of the region is uniform. Despite this simplification, our results should be correct to within an order of magnitude.

A typical sight line through the Galaxy could intersect several O VI regions, each of which would contribute differently to the total O VI column density and intensity. Because we lack the spectral resolution to isolate the contributions of individual regions, we must identify cases in which the integrated O VI column density and intensity can be attributed to a single region. The likelihood that absorption and emission sight lines probe the same O VI region is highest for nearby stars: at a distance of 100 pc, the 3/5 offset between the *FUSE* LWRs and MDRS apertures corresponds to ~ 0.1 pc. Moreover, sight lines to nearby stars are more likely to intersect only a single interface or transition region than sight lines to distant objects. We discuss one such sight line in §6.1. For more distant emitting regions, such as the HVCs discussed in §6.2, we equate the absorbing and emitting gas based on their velocities and consider the range of reported O VI column densities for the HVC.

6.1. O VI-Bearing Gas in the Galactic Disk

Four of our 3σ sight lines correspond to nearby white dwarfs in the O VI absorption-line survey of Savage & Lehner (2006). Their O VI absorption-line measurements and our O VI emission-line velocities are presented in Table 5. (Note that the velocities in Table 5 are heliocentric.) The best case in our sample for combining emission and absorption measurements is sight line P20411. The velocity of its O VI emission ($v_{\text{Helio}} = -6 \pm 15$ km s $^{-1}$) is consistent with that of the O VI absorption ($v_{\text{Helio}} = -3.8 \pm 3.6$ km s $^{-1}$; Savage & Lehner 2006) measured toward WD 0004+330 (GD 2), a DA white dwarf at a distance of 97 pc (Vennes et al. 1997). The relative narrowness of the O VI emission feature (the best-fit value of the intrinsic Gaussian FWHM is 60 ± 40 km s $^{-1}$) suggests that it probes a single emitting region. P20411 was observed with the MDRS aperture centered on the star, so the LWRs aperture probes a sight line

passing within ~ 0.1 pc of the white dwarf.

The spectrum of GD 2 shows absorption from molecular hydrogen with a column density $\log N(\text{H}_2) = 14.46$ (cm $^{-2}$; Lehner et al. 2003). Since H_2 is assumed to form on dust grains, we must consider the possibility of dust extinction along this line of sight. To estimate the extinction toward this star, we compare it with HZ 43, another nearby DA white dwarf that shows no H_2 absorption. Finley, Koester, & Basri (1997) derive effective temperatures of 49,360 and 50,822 K for GD 2 and HZ 43, respectively. If their temperatures are nearly equal, then any difference in their $B-V$ colors is likely due to reddening toward GD 2. These colors are -0.29 and -0.31 magnitudes for GD 2 and HZ 43, respectively (Eggen 1968; Bohlin et al. 2001), meaning that $E(B-V) = 0.02$ toward GD 2, which corresponds to an attenuation of 30% at 1032 Å (Fitzpatrick 1999). More recent analyses suggest that GD 2 is somewhat cooler than HZ 43 (for example, Barstow et al. 2003 derive temperatures of 45,460 and 46,196 K from the star's Balmer and Lyman lines, respectively), which would explain the color difference without invoking dust, so we will treat this reddening as an upper limit.

The observed O VI $\lambda 1032$ intensity is 2100 LU and the absorbing column is $N(\text{O VI}) = 6.2 \times 10^{12}$ cm $^{-2}$. We assume that the intrinsic intensity of the O VI $\lambda 1038$ emission is half that of the 1032 Å line, as would be expected if the gas were optically thin. Assuming a temperature of 2.8×10^5 K, Equation 5 from Shull & Slavin (1994) yields an electron density $n_e = 0.22$ cm $^{-3}$ if $E(B-V) = 0.00$ and $n_e = 0.29$ cm $^{-3}$ if $E(B-V) = 0.02$. The O VI absorption line has a Doppler parameter $b \sim 30$ km s $^{-1}$; if thermal, it implies a temperature of 4.2×10^5 K, which does not change the derived electron density.

To calculate the O VI density and the path length through the emitting region, we need the oxygen abundance and the fraction of oxygen in O $^{+5}$. Oliveira et al. (2005) derive a mean O/H ratio for the Local Bubble of $(3.45 \pm 0.19) \times 10^{-4}$. For plasmas in collisional ionization equilibrium, the O $^{+5}$ fraction peaks at 22% when the gas temperature is 2.8×10^5 K (Sutherland & Dopita 1993). With these values, and assuming that the gas is completely ionized ($n_e = 1.2n_{\text{H}}$), we derive an O VI density of 1.4×10^{-5} cm $^{-3}$ and a path length through the gas of $\sim 4.4 \times 10^{17}$ cm or 0.14 pc for zero reddening. If $E(B-V) = 0.02$, the O VI density and the path length through the gas become 1.8×10^{-5} cm $^{-3}$ and 0.11 pc, respectively.

Savage & Lehner (2006) report that the O VI absorption feature in the spectrum of GD 2 is well detected (4.8σ) and closely aligned in velocity with the C II and O I absorption, consistent with O VI formation in a condensing interface between the cool gas traced by the C II and O I and a hot exterior gas. Böhringer & Hartquist (1987) model conductive interfaces around spherical interstellar clouds embedded in a hot interstellar medium. One of their models (model H) assumes a cloud of radius 3×10^{17} cm in an external medium of temperature 5×10^5 K. The model predicts a particle density at the cloud surface of $n_0 = 0.73$ cm $^{-3}$ (our mean cloud density is $n = 0.40$ cm $^{-3}$), a column density through the interface region of $N(\text{O VI}) = 3.2 \times 10^{12}$ cm $^{-2}$, and a mean temperature for the O $^{+5}$ ions of 4.7×10^5 K. These predictions are within a factor of 2 of our derived cloud

parameters. The high temperature is a general feature of the Böhringer & Hartquist models.

Another white-dwarf sight line worthy of comment is P10411 (WD 0455–282). While the velocities of its principal O VI emission and absorption components disagree, Holberg, Barstow, & Sion (1998) report Si IV and C IV absorption in *IUE* spectra of this star at $v_{\text{Helio}} = 16.21 \pm 2.66 \text{ km s}^{-1}$, and Savage & Lehner (2006) report weak O VI absorption at the same velocity. Holberg et al. argue that this absorption is circumstellar, rather than interstellar. If so, the emission that we observe at $v_{\text{Helio}} = 7 \pm 9 \text{ km s}^{-1}$ may come from this circumstellar material. With an effective temperature $T_{\text{eff}} = 57,200 \text{ K}$, the white dwarf is too cool to produce O^{+5} through photoionization, so the emission must be powered by shocks in the circumstellar material, perhaps generated by the interaction of material from previous episodes of mass loss. This mechanism is at work in planetary nebulae (Villaver et al. 2002), and high-ionization lines have been observed in the spectra of low- T_{eff} central stars of planetary nebulae (J. Herald, private communication).

6.2. O VI-Bearing Gas in High-Velocity Clouds

Two of our high-velocity sight lines, B12901 and S40549, intersect known H I HVCs and share the clouds' velocities (§ 5.3). Data set B12901 consists of spectra obtained along three closely-spaced sight lines that probe the Magellanic Stream, but only one of them, I2050501/I2050510, exhibits significant O VI $\lambda 1032$ emission (§ A.2). Its LSR velocity is $206 \pm 13 \text{ km s}^{-1}$, and its intensity is $3000 \pm 600 \text{ LU}$ (Table 6). The O VI column densities of HVCs associated with the positive-velocity portion of the Magellanic Stream range from $\log N = 13.78$ to 14.33 . Their velocities range from 183 to 330 km s^{-1} with a mean of 232 km s^{-1} (Sembach et al. 2003). Combining these absorption and emission measurements, we derive an electron density for the O VI-bearing gas of $0.01\text{--}0.03 \text{ cm}^{-3}$. Adopting the LMC oxygen abundance (2.24×10^{-4} O atoms per H atom; Russell & Dopita 1992), we find a path length through the emitting gas of $16\text{--}200 \text{ pc}$.

Sight line S40549, with $v_{\text{LSR}} = -172 \pm 9 \text{ km s}^{-1}$ and $I(1032) = 8200 \pm 2300 \text{ LU}$, probes Complex C, a large assembly of high-velocity ($-170 \lesssim v_{\text{LSR}} \lesssim -100 \text{ km s}^{-1}$) H I in the northern Galactic sky between $l \sim 30^\circ$ and $l \sim 150^\circ$. Measured O VI column densities for sight lines through Complex C range from $\log N = 13.67$ to 14.22 (Sembach et al. 2003). From these values, we derive an electron density for the O VI-bearing gas of $0.03\text{--}0.11 \text{ cm}^{-3}$. Assuming a Galactic O/H ratio of 6.61×10^{-4} (Allen 1973), we find a path length through the emitting gas of $1.1\text{--}14 \text{ pc}$. The color excess toward S40549 is $E(B-V) = 0.02$ (Table 3), which attenuates emission at 1032 \AA by 30% (Fitzpatrick 1999). Correcting for this attenuation raises the electron density and reduces the path length through the emitting gas by the same factor. We expect the extinction along sight line B12901 to be similar, as the reddening in this region is patchy and quite low along nearby sight lines (§ A.2).

The emitting regions probed by sight lines B12901 and S40549 appear to span an order of magnitude in n_e and two orders of magnitude in path length. While this spread may reflect real variations in the properties of

thick disk/halo gas, we should note that S40549 is one of the shortest exposures in our sample. Its O VI $\lambda 1032$ feature is both extremely narrow ($\text{FWHM} = 2 \pm 20 \text{ km s}^{-1}$) and unusually bright. Careful analysis confirms that this feature is statistically significant at the 3σ level; however, additional exposure time would be helpful to confirm this result.

6.3. Limits on the Gas Density

Along sight lines through the Galactic disk, most of the O VI column densities measured to date lie in the range $\log N(\text{O VI}) = 12.6$ to 14.0 , and along sight lines through the Galactic halo, in the range $\log N(\text{O VI}) = 13.7$ to 14.7 (Savage et al. 2003). Excluding emission associated with known SNRs and the short S40549 exposure discussed in § 6.2, our O VI $\lambda 1032$ intensities also span a narrow range, from 1800 to 5500 LU . (The lower bound reflects our sensitivity limits.) The restricted range of observed column densities, together with the narrow range of our measured intensities, suggests that the volume densities of the O VI-bearing gas are likewise limited. We have found two flavors of O VI-bearing gas: narrow interfaces in the Galactic disk with densities of about 0.1 cm^{-3} and more extended cooling regions in the Galactic halo with densities of about 0.01 cm^{-3} . We argue that, in general, the volume densities of O VI-bearing gas in the Galactic disk and halo are unlikely to differ significantly from our derived values. Indeed, the observed range of O VI intensities is consistent with a constant volume density in each environment, with O VI column density as the only variable. In particular, our observations rule out the general presence of O VI-bearing thermal interfaces or cooling regions with densities of 1 to 10 cm^{-3} or greater.

Our observations do not rule out the presence of hot, low-density gas with significant O VI column densities. Heckman et al. (2002) have shown that, for radiatively cooling gas, the O VI column density at a temperature of $2 \times 10^6 \text{ K}$ is comparable with that at $3 \times 10^5 \text{ K}$ because, though the O VI fraction is smaller at the higher temperature, the cooling times are much longer. The O VI emission from such regions would be too weak for detection by *FUSE* because their emission measure would be too low.

7. SUMMARY

We have conducted a survey of diffuse O VI $\lambda 1032$ emission in the Galaxy using archival data from the *Far Ultraviolet Spectroscopic Explorer (FUSE)*. Of our 183 sight lines, 29 show O VI emission at 3σ significance. Measured intensities range from 1800 to 9100 LU , with a median of 3300 LU . An additional 35 sight lines provide upper limits of 2000 LU or less. Though the presence of O VI emission along low-latitude, high-extinction sight lines suggests that these emitting regions are nearby (probably within a few hundred parsecs), other emitting regions are more likely to be associated with HVCs in the Galactic halo.

Analysis of 21 low-velocity, low-intensity, 3σ emission features reveals that the O VI-emitting regions at high latitudes are intrinsically fainter than those at low latitudes and may represent a distinct population of emitters. Line velocities are generally consistent with a simple model of Galactic rotation. Some of the O VI-

emitting regions appear to have angular sizes smaller than the *FUSE* LWRS aperture, which places a distance-dependent constraint on their physical size. By combining emission and absorption measurements through the same O VI-bearing regions, we find evidence for relatively narrow, high-density conductive interfaces in the local ISM and more extended, low-density regions in HVCs. Based on the narrow range of O VI intensities in our sample and of O VI column densities in the Galactic disk and halo, we argue that the volume densities of O VI-bearing regions in each environment are unlikely to differ significantly from our derived values.

The authors thank Ricardo Velez for his assistance with the initial data reduction for this project. We acknowledge with gratitude the ongoing efforts of the *FUSE* P.I. team to make this mission successful. R. S.

thanks J. Cuervo for interesting discussions about statistical methods and for help with their implementation in STATA. This research has made use of the NASA/IPAC Extragalactic Database (NED), which is operated by the Jet Propulsion Laboratory, California Institute of Technology, under contract with the National Aeronautics and Space Administration; the NASA Astrophysics Data System (ADS); and the Multimission Archive at the Space Telescope Science Institute (MAST). STScI is operated by the Association of Universities for Research in Astronomy, Inc., under NASA contract NAS5-26555. Support for MAST for non-HST data is provided by the NASA Office of Space Science via grant NAG5-7584 and by other grants and contracts. This work is supported by NASA grant NAS5-32985 to the Johns Hopkins University.

APPENDIX

A. NOTES ON INDIVIDUAL LINES OF SIGHT

A.1. *P12011 and P12012 (Jupiter)*

Our sample includes two observations of Jupiter (P12011 and P12012) designed to search for HD fluorescently pumped by solar Lyman β emission. In both cases, the MDRS aperture was centered on the planet, and the LWRS aperture was offset by 3.5 arcmin (or 10.3 Jupiter radii) in a direction perpendicular to the plane of the Jovian system. No O VI emission is present in the P12012 spectrum ($\alpha = 07:06:57.55$, $\delta = +22:24:10.1$, J2000), but a 3σ feature is seen in P12011 ($\alpha = 07:06:36.64$, $\delta = +22:24:32.0$). The heliocentric velocity of the P12011 feature is -0.2 ± 25 km s $^{-1}$, suggesting that the emission may have a local origin. If it were scattered solar O VI emission, we would expect to see emission from C III $\lambda 977$ as well, but none is present in the SiC 2A spectrum from this observation. Another possibility is that the observed emission is due to H $_2$ fluorescence, but comet spectra that show strong H $_2$ fluorescence near 1032 Å also exhibit a strong 1163.7 Å line (P. D. Feldman 2005, private communication), which is not seen in the LiF 1B spectrum from this observation. We conclude that the observed O VI is of interstellar origin.

A.2. *B12901*

The *FUSE* observations of sight line B12901 were originally designed as a shadowing experiment to search for O VI emission arising in the Local Bubble (Shelton 2003). This sight line intersects a diffuse interstellar filament at a distance of 230 ± 30 pc (Penprase et al. 1998), well beyond the ~ 100 pc radius of the Local Bubble (Snowden et al. 1998). As its mean color excess is $E(B - V) = 0.17 \pm 0.05$ (Penprase et al. 1998), it was assumed that any O VI emission would have to come from material closer than the filament, presumably the Local Bubble itself.

We detect an O VI $\lambda 1032$ emission feature of some 3σ significance in this spectrum, but with a velocity $v_{\text{LSR}} = 192 \pm 19$ km s $^{-1}$, the emission is unlikely to originate in either the Local Bubble or the intervening filament. O VI $\lambda 1032$ absorption features in the spectra of nearby white dwarfs exhibit velocities $|v| < 40$ km s $^{-1}$ (relative to the ISM as defined by the C II $\lambda 1036$ line; Oegerle et al. 2005), and neutral gas in the filament moves at $0 < v_{\text{LSR}} < 10$ km s $^{-1}$ (Penprase et al. 1998). Penprase et al. find that the filament is patchy, with $E(B - V) \leq 0.01$ toward some background stars. Maps of the high-velocity H I sky published by Sembach et al. (2003) and Wakker et al. (2003) reveal that sight line B12901 probes an HVC with $v_{\text{LSR}} \sim 200$ km s $^{-1}$ that is associated with the Magellanic Stream. We conclude that the observed emission is produced by O VI-bearing gas associated with the HVC.

Data set B12901 consists of five observations (Table 2) along three closely-spaced sight lines. Since the filament is patchy, we searched for O VI emission along each sight line separately, using the technique described in § 4. Our results are presented in Table 6: we find a strong O VI $\lambda 1032$ feature in the combined I2050501/I2050510 spectrum and can set only upper limits on emission in the I2050601 and combined B1290101/B1290102 spectra. The two I205 sight lines are separated by approximately $30''$. The strong variation in O VI intensity over such small angular scales is consistent with a patchy distribution of extinction in the filament.

In her original analysis, Shelton (2003) found no evidence for O VI emission in these data and placed a 2σ upper limit of 530 LU on the intensity of the O VI $\lambda 1032$ line. Excluding the observed O VI $\lambda 1032$ emission feature, we derive a 2σ upper limit of 600 LU for the full B12901 data set. Shelton's conclusions about the physical conditions within the Local Bubble are therefore unchanged by our result.

REFERENCES

- Allen, C. W. 1973, *Astrophysical Quantities* (3rd ed.; London: Athlone Press)
- Andersson, B.-G., Knauth, D. C., Snowden, S. L., Shelton, R. L., & Wannier, P. G. 2004, *ApJ*, 606, 341
- Barstow, M. A., Good, S. A., Burleigh, M. R., Hubeny, I., Holberg, J. B., & Levan, A. J. 2003, *MNRAS*, 344, 562
- Bohlin, R. C., Dickinson, M. E., & Calzetti, D. 2001, *AJ*, 122, 2118
- Böhringer, H. & Hartquist, T. W. 1987, *MNRAS*, 228, 915

- Bowen, D. V., Jenkins, E. B., Tripp, T. M., Sembach, K. R., & Savage, B. D. 2006, in ASP Conf. Ser. 348, *Astrophysics in the Far Ultraviolet: Five Years of Discovery with FUSE*, ed. G. Sonneborn, H. W. Moos, & B.-G. Andersson (San Francisco: ASP), 412
- Dixon, W. V., Sallmen, S., Hurwitz, M., & Lieu, R. 2001, *ApJ*, 552, L69
- Eggen, O. J. 1968, *ApJS*, 16, 97
- Finley, D. S., Koester, D., & Basri, G. 1997, *ApJ*, 488, 375
- Fitzpatrick, E. L. 1999, *PASP*, 111, 63
- Haffner, L. M., Reynolds, R. J., Tufte, S. L., Madsen, G. J., Jaehnig, K. P., & Percival, J. W. 2003, *ApJS*, 149, 405
- Heckman, T. M., Norman, C. A., Strickland, D. K., & Sembach, K. R. 2002, *ApJ*, 577, 691
- Holberg, J. B., Barstow, M. A., & Sion, E. M. 1998, *ApJS*, 119, 207
- Howk, J. C., Savage, B. D., Sembach, K. R., & Hoopes, C. G. 2002, *ApJ*, 572, 264
- Korpela, E. J. et al. 2006, *ApJ*, in press (astro-ph/0601583)
- Kriss, G. A. 1994, in ASP Conf. Ser. 61, *Astronomical Data Analysis Software and Systems III*, ed. D. R. Crabtree, R. J. Hanisch, & J. Barnes (San Francisco: ASP), 437
- Lehner, N., Jenkins, E. B., Gry, C., Moos, H. W., Chayer, P., & Lacour, S. 2003, *ApJ*, 595, 858
- Martin, C. & Bowyer, S. 1990, *ApJ*, 350, 242
- Moos, H. W. et al. 2000, *ApJ*, 538, L1
- Murphy, E. M. et al. 2000, *ApJ*, 538, L35
- Oegerle, W. R., Jenkins, E. B., Shelton, R. L., Bowen, D. V., & Chayer, P. 2005, *ApJ*, 622, 377
- Oliveira, C. M., Dupuis, J., Chayer, P., & Moos, H. W. 2005, *ApJ*, 625, 232
- Otte, B. & Dixon, W. V. 2006, *ApJ*, submitted
- Otte, B., Dixon, W. V., & Sankrit, R. 2003, *ApJ*, 586, L53
- , 2004, *ApJ*, 606, L143
- Penprase, B. E., Lauer, J., Aufrecht, J., & Welsh, B. Y. 1998, *ApJ*, 492, 617
- Press, W. H., Flannery, B. P., Teukolsky, S. A., & Vetterling, W. T. 1988, *Numerical Recipes in C: The Art of Scientific Computing* (Cambridge: University Press, 1988)
- Russell, S. C. & Dopita, M. A. 1992, *ApJ*, 384, 508
- Sahnou, D. J. et al. 2000, *ApJ*, 538, L7
- Savage, B. D. 1995, in ASP Conf. Ser. 80: *The Physics of the Interstellar Medium and Intergalactic Medium*, 233
- Savage, B. D. & Lehner, N. 2006, *ApJS*, 162, 134
- Savage, B. D., Sembach, K. R., Wakker, B. P., Richter, P., Meade, M., Jenkins, E. B., Shull, J. M., Moos, H. W., & Sonneborn, G. 2003, *ApJS*, 146, 125
- Schlegel, D. J., Finkbeiner, D. P., & Davis, M. 1998, *ApJ*, 500, 525
- Sembach, K. R. et al. 2000, *ApJ*, 538, L31
- , 2003, *ApJS*, 146, 165
- Shelton, R. L. 2002, *ApJ*, 569, 758
- , 2003, *ApJ*, 589, 261
- Shelton, R. L. et al. 2001, *ApJ*, 560, 730
- Shull, J. M. & Slavin, J. D. 1994, *ApJ*, 427, 784
- Shull, J. M. et al. 2000, *ApJ*, 538, L73
- Snowden, S. L., Egger, R., Finkbeiner, D. P., Freyberg, M. J., & Plucinsky, P. P. 1998, *ApJ*, 493, 715
- Snowden, S. L. et al. 1997, *ApJ*, 485, 125
- Sternberg, A. 1989, *ApJ*, 347, 863
- Sutherland, R. S. & Dopita, M. A. 1993, *ApJS*, 88, 253
- Vennes, S., Thejll, P. A., Galvan, R. G., & Dupuis, J. 1997, *ApJ*, 480, 714
- Villaver, E., Manchado, A., & García-Segura, G. 2002, *ApJ*, 581, 1204
- Wakker, B. P. et al. 2003, *ApJS*, 146, 1
- Welsh, B. Y., Sallmen, S., Sfeir, D., Shelton, R. L., & Lallement, R. 2002, *A&A*, 394, 691

TABLE 2
FUSE OBSERVATIONS CONTRIBUTING TO EACH SURVEY SIGHT LINE

Sight Line	<i>FUSE</i> Observation ID's				
A01002	A0100201				
A03406	A0340601				
A03407	A0340701				
A04604	A0460404				
A04802	A0480202				
A05101	A0510102				
A09401	A0940102				
A10001	A1000101				
A11701	A1170101				
A11703	A1170303	A1170404			
A13902	A1390201	A1390202	A1390203	A1390204	A1390205
B00302	B0030201				
B00303	B0030301				
B01802	B0180201				
B01805	B0180501	B0180502			
B04604	B0460401	B0460501			
B06801	B0680101				
B12901	B1290101	B1290102	I2050501	I2050510	I2050601
C02201	C0220101	C0220102			
C02301	C0230101				
C03701	C0370101				
C03702	C0370201	C0370202	C0370203	C0370204	C0370205 C0370206
C06401	C0640101	C0640201	C0640301		
C07601	C0760101	C0760201	C0760301	C0760401	
C10101	C1010101	C1010201	C1010301	C1010302	S4058501
C10503	C1050301	C1050302	C1050303	C1050304	
C11602	C1160202				
C11603	C1160301	C1160402			
C16501	C1650101	C1650102	C1650103	C1650104	C1650105 C1650106 C1650107 P1040701
D04001	D0400101				
D05801	D0580101				
D05802	D0580201				
D11701	D1170101	D1170102	D1170103		
D12001	D1200101				
D12003	D1200301				
D12006	D1200601	D1201601			
D12008	D1200801				
D12017	D1201701				
D15801	D1580101	D1580102			
D90301	D9030101				
D90302	D9030201	D9030202			
D90305	D9030501				
E12101	E1210101	E1210201			
I20509	I2050901				
M10103	M1010301				
M10704	M1070414	M1070415	M1070420	M1070421	M1070423 M1070424 M1070427 S4050201 S4050202 S4050204
P10409	P1040901				
P10411	P1041101	P1041102	P1041103		
P10414	P1041403				
P10418	P1041801	S5053701			
P10420	P1042003	S4050903	S4050904		
P10421	P1042101	P1042105	S4050501	S4050502	S4050503 S4050504 S5130201
P10425	P1042501	P1042601			
P10429	P1042901	P1042902	S4057901	S4057902	S4057903 S4057904 S4057905 S5054401
P11003	P1100301	P1100302			
P11607	P1160701				
P12011	P1201112				
P12012	P1201213				
P19802	P1980202				
P20406	P2040601				
P20408	P2040802	P2040803	S4050801		
P20410	P2041002	S4053601			
P20411	P2041102	P2041103	P2041104		
P20419	P2041901				
P20421	P2042101				
P20422	P2042201	P2042202	P2042203	S4055602	S4055603 S4055607 S4055608 S4055609
P20423	P2042301				
P20516	P2051602	P2051603	P2051604	P2051605	P2051606 P2051607 P2051608 P2051609 S4055701 S4055702
	S4055703	S4055704	S4055705	S4055707	
	P2051701	P2051702	P2051703		
P20517	P3020802				
P30208	P3031401	P3031402			
P30314	Q1080303				
Q10803	Q1100201				
Q11002	S1010206	S1010207	S4056301	S4056302	S4056303 S4056304 S4056305 S4056306 S4056307
S10102	S3040203	S3040204	S3040205	S3040206	S3040207 S3040208 S4059601 S4059602
S30402	S4050101	S4050103			
S40501	S4050401				
S40504	S4050601				
S40506	S4050701				
S40507	S4051001	S4051002			
S40510	S4051201				
S40512	S4051301				
S40513	S4051401	S4051402			
S40514	S4051501	S4051502			
S40515	S4051802	S4051803	S4051804	S4051805	
S40518	S4052101				
S40521	S4052201				
S40522	S4052301	S4052302			
S40523	S4052402	S4052403	S4052404	S4052405	S4052406
S40524	S4052501				
S40525	S4052601				
S40526	S4052801	S4052802			
S40528	S4052901	S4052902			
S40529	S4053101				
S40531	S4053201	S4053202	S5053201		
S40532	S4053301	S4053302			
S40533	S4053401				
S40534	S4053501				
S40535	S4053701	S4053702			
S40537	S4054001	S4054002	S4054003	S4054004	S4054005
S40540	S4054101				
S40541	S4054201				
S40542	S4054301				
S40543	S4054801				
S40548	S4054901	S4054902			
S40549	S4055001	S4058001			
S40550					

TABLE 2 — *Continued*

Sight Line	FUSE Observation ID's				
S40552	S4055201				
S40553	S4055301				
S40555	S4055501	S4055502	S4055503	S4055504	
S40558	S4055801				
S40559	S4055901				
S40560	S4056001	S4056002	S4058401		
S40561	S4056101				
S40562	S4056201				
S40564	S4056401				
S40565	S4056501	S4056502			
S40566	S4056601	S4056602	S4056603	S4056604	
S40568	S4056801	S4056802			
S40570	S4057001	S4057002			
S40572	S4057201				
S40573	S4057301	S4057302	S4057303	S5220101	
S40574	S4057401				
S40577	S4057701				
S40581	S4058101	S4058102			
S40582	S4058201	S4058202	S4058203	S5054101	
S40583	S4058301				
S40587	S4058701				
S40588	S4058801				
S40589	S4058901				
S40590	S4059001				
S40594	S4059401				
S50502	S4057601	S4057602	S4057603	S4057604	S5050201 S5050202 S5230601
S50504	S5050402	S5050403			
S50505	S5050501				
S50506	S5050601				
S50507	S5050701				
S50508	S5050801				
S50509	S5050901	S5050902			
S50510	S5051001	S5051101			
S50512	S5051201				
S50514	S5051401				
S50515	S5051501				
S50516	S5051601				
S50517	S5051701				
S50518	S5051801	S5052101			
S50522	S5052201				
S50523	S5052301				
S50525	S5052501				
S50527	S5052701				
S50529	S5052901				
S50530	S5053001				
S50533	S5053301				
S50536	S5053601				
S50538	S5053801				
S50539	S5053901				
S50540	S5054001				
S50542	S5054201				
S50543	S5054301				
S51303	S5130301				
S51401	S5140102				
S51601	S4051701	S4059101	S5160101		
S52001	S5200101				
S52301	S5050101	S5050102	S5050103	S5230101	S5230102 S5230201 S5230202 S5230301 S5230302 S5230401
	S5230402	S5230501	S5230502	S5230503	S5230504 S5230505 S5230506 S5230507 S5230508
	S5051301	S5051302	S5230703	S5230704	
S52307	S5230901				
S52309	S5230901				
Z90702	Z9070201				
Z90706	Z9070601				
Z90708	Z9070801				
Z90709	Z9070901				
Z90711	Z9071101				
Z90712	Z9071201				
Z90714	Z9071401				
Z90715	Z9071501				
Z90719	Z9071901				
Z90721	Z9072101				
Z90722	Z9072201				
Z90725	Z9072501				
Z90726	Z9072601	Z9072602			
Z90727	Z9072701				
Z90733	Z9073301				
Z90735	Z9073501				
Z90736	Z9073601				
Z90737	Z9073701	Z9073702			

TABLE 3
O VI $\lambda 1032$ DETECTIONS

Sight Line	Target Name ^a	l (deg)	b (deg)	t^b (s)	Bin ^c	Intensity ^d (10^3 LU)	Wavelength ^e (Å)	FWHM ^f (km s^{-1})	v_{LSR} (km s^{-1})	$E(B - V)^g$ (mag)	SXR ^h (RU)	H_α ⁱ (10^3 LU)
3 σ Detections												
A04604	NGC5253	314.9	30.1	18252	14	4.5 ± 1.4	1031.93 ± 0.08	150 ± 70	2 ± 22	0.056	820 ± 40	134 ± 3
A11703	Virgo	284.0	74.5	10931	8	3.7 ± 1.2	1031.95 ± 0.06	60 ± 20	9 ± 18	0.023	4520 ± 90	...
B12901	SKY-033255-632751	278.6	-45.3	83579	8	2.0 ± 0.6	1032.64 ± 0.06	110 ± 70	192 ± 19	0.160	590 ± 40	...
C06401	NGC5846	0.4	48.8	39127	8	2.9 ± 0.8	1031.46 ± 0.05	40 ± 40	-122 ± 13	0.056	740 ± 50	65 ± 3
C07601	NGC6752	336.5	-25.6	56225	8	1.8 ± 0.4	1031.87 ± 0.02	6 ± 10	-17 ± 6	0.056	490 ± 80	...
C10503	MS2318.2-4220	348.1	-66.3	97954	8	1.8 ± 0.4	1031.92 ± 0.05	90 ± 40	-5 ± 13	0.021	880 ± 70	...
C16501	HD22049	195.8	-48.1	85441	8	2.1 ± 0.5	1031.97 ± 0.04	50 ± 50	-2 ± 11	0.039	1470 ± 60	476
D04001	NGC625	273.7	-73.1	43428	8	2.6 ± 0.8	1032.03 ± 0.06	90 ± 50	19 ± 18	0.016	1040 ± 40	...
D90305	Fairall 917	346.6	-39.5	21796	14	5.5 ± 1.5	1031.96 ± 0.08	180 ± 50	11 ± 24	0.035	790 ± 50	...
I20509	Background	315.0	-41.3	93437	8	3.3 ± 0.6	1032.05 ± 0.05	170 ± 40	26 ± 16	0.036	890 ± 60	...
P10411	WD0455-282	229.3	-36.2	46240	8	4.3 ± 0.9	1031.95 ± 0.03	60 ± 40	-12 ± 9	0.023	900 ± 40	211 ± 3
P10414	HD039659	166.2	10.5	7969	8	3.2 ± 1.0	1031.14 ± 0.02	3 ± 20	-231 ± 7	0.233	320 ± 30	365 ± 3
P10429	WD1631+781	111.3	33.6	90149	8	2.9 ± 0.8	1031.71 ± 0.14	300 ± 50	-50 ± 40	0.039	583 ± 22	56 ± 3
P12011	JUP-DTOH1	194.3	13.2	4731	14	8.8 ± 2.4	1031.94 ± 0.10	200 ± 40	-8 ± 28	0.056	1030 ± 40	352 ± 3
P20411	WD0004+330	112.5	-28.7	48131	8	2.1 ± 0.6	1031.90 ± 0.05	60 ± 40	-1 ± 15	0.049	290 ± 40	115 ± 3
P20422	WD2004-605	336.6	-32.9	76972	8	4.8 ± 0.6	1031.91 ± 0.03	130 ± 30	-7 ± 8	0.049	880 ± 80	...
P20516	LSE 44	313.4	13.5	85811	8	3.5 ± 0.6	1031.83 ± 0.04	100 ± 20	-28 ± 12	0.124	490 ± 50	...
S30402	HD224151	115.4	-4.6	52925	8	2.9 ± 0.9	1032.65 ± 0.12	210 ± 80	217 ± 34	0.691	325 ± 22	1054
S40506	HD093840-BKGD	282.1	11.1	12962	8	4.0 ± 1.3	1031.91 ± 0.05	20 ± 100	-14 ± 13	0.167	650 ± 40	...
S40543	NCVZ-BKGD	100.8	44.8	13915	8	3.1 ± 1.0	1032.65 ± 0.05	30 ± 20	224 ± 16	0.031	960 ± 30	31
S40548	CVZ-BKGD	95.4	36.1	98216	8	2.8 ± 0.6	1031.82 ± 0.05	150 ± 40	-15 ± 15	0.024	939 ± 14	81
S40549	NCVZ-BKGD	107.0	48.8	2406	14	8.2 ± 2.3	1031.29 ± 0.03	2 ± 20	-172 ± 9	0.021	1121 ± 23	48 ± 3
S40560	WD1725+586-BKGD	87.2	33.8	22975	8	4.2 ± 1.4	1031.82 ± 0.06	110 ± 90	-13 ± 16	0.037	756 ± 19	106 ± 4
S40590	HE2-138-BKGD	319.7	-9.4	10816	8	3.3 ± 0.9	1031.77 ± 0.02	3 ± 10	-49 ± 5	0.109	410 ± 40	...
S50504	HD003827-BKGD	120.8	-23.2	14137	8	4.4 ± 0.9	1031.86 ± 0.02	3 ± 40	-15 ± 7	0.063	560 ± 30	224
S50508	LS982-BKGD	257.1	-3.9	10515	8	9.1 ± 1.8	1031.97 ± 0.03	30 ± 30	-4 ± 8	1.260	670 ± 30	...
S50509	HD26976-BKGD	200.8	-38.0	16931	14	4.9 ± 1.4	1031.84 ± 0.09	190 ± 50	-41 ± 27	0.096	1160 ± 50	364
S50510	WD0232+035-BKGD	166.0	-50.3	34523	8	2.2 ± 0.6	1031.80 ± 0.03	6 ± 30	-45 ± 8	0.043	570 ± 40	61 ± 3
Z90715	2MASXJ1622346+735943	106.8	35.3	14596	14	4.4 ± 1.4	1031.92 ± 0.09	160 ± 70	13 ± 27	0.031	685 ± 20	78 ± 3
2 σ Detections												
A09401	Mrk153	156.7	56.0	20589	14	3.2 ± 1.3	1031.86 ± 0.10	140 ± 100	-14 ± 30	0.013	1000 ± 30	22 ± 3
A10001	ALPHA-TRA	321.5	-15.3	9409	14	2.7 ± 1.3	1031.82 ± 0.13	100 ± 20	-35 ± 38	0.105	500 ± 60	...
B00302	REJ-1043+490	162.7	57.0	28618	14	2.6 ± 1.0	1031.92 ± 0.17	230 ± 80	2 ± 49	0.013	1110 ± 40	15 ± 3
B00303	REJ-1059+514	156.3	57.8	24823	8	2.9 ± 1.0	1031.70 ± 0.14	200 ± 40	-60 ± 42	0.011	1140 ± 40	...
B01802	NGC604	133.8	-31.2	5940	14	7.4 ± 4.9	1032.53 ± 0.32	270 ± 230	176 ± 93	0.046	440 ± 30	130 ± 3
C10101	NGC6543-N-extension	96.5	30.0	35164	8	3.1 ± 1.5	1031.71 ± 0.19	260 ± 140	-46 ± 55	0.045	529 ± 4	1588 ± 4
D05802	WD1528+487	78.9	52.7	12136	14	6.8 ± 2.5	1031.99 ± 0.15	200 ± 30	33 ± 44	0.013	1260 ± 40	25 ± 3
D12001	IC289	138.8	2.8	5464	8	5.4 ± 2.5	1031.90 ± 0.10	80 ± 60	-5 ± 30	1.208	410 ± 30	836 ± 4
D12006	NGC6826-POS2	83.6	12.8	5108	14	3.0 ± 2.0	1032.19 ± 0.11	20 ± 210	92 ± 33	0.111	515 ± 18	1470 ± 4
D12008	NGC7354	107.8	2.3	3009	14	6.6 ± 3.1	1033.00 ± 0.14	100 ± 30	323 ± 41	2.207	364 ± 23	1432 ± 4
E12101	R-Aqr-jet-NE	66.5	-70.3	20959	14	4.4 ± 2.3	1033.58 ± 0.32	450 ± 180	478 ± 92	0.025	590 ± 40	...
P10418	HD61421	213.7	13.0	13934	14	4.5 ± 1.8	1031.84 ± 0.08	130 ± 90	-40 ± 24	0.061	600 ± 40	240
P10420	WD1034+001	247.6	47.8	14964	8	3.0 ± 1.3	1032.50 ± 0.07	30 ± 30	159 ± 19	0.075	550 ± 30	228 ± 4
P11003	HS1307+4617	113.0	70.7	43176	8	1.3 ± 0.5	1031.71 ± 0.10	100 ± 40	-51 ± 30	0.009	990 ± 40	37 ± 2
P20408	WD1211+332	175.0	80.0	19616	14	3.2 ± 1.5	1031.92 ± 0.11	140 ± 100	5 ± 31	0.012	1040 ± 40	35
P20410	WD1800+685	98.7	29.8	19737	8	2.7 ± 1.1	1031.84 ± 0.08	80 ± 60	-10 ± 24	0.056	613 ± 7	115 ± 3
P20423	WD2156-546	339.7	-48.1	4403	14	6.6 ± 4.5	1032.61 ± 0.31	250 ± 220	196 ± 91	0.025	2020 ± 60	...
P20517	LS 1274	277.0	-5.3	35945	8	4.9 ± 1.7	1031.81 ± 0.15	290 ± 120	-47 ± 45	0.550	400 ± 30	...
P30314	REJ1738+66	96.9	32.0	21810	8	2.5 ± 0.9	1031.84 ± 0.06	30 ± 30	-8 ± 17	0.044	614 ± 7	128 ± 3
Q11002	HD125162	87.0	64.7	8203	14	8.2 ± 3.3	1031.81 ± 0.31	450 ± 110	-21 ± 91	0.010	1270 ± 30	33
S40504	NGC2392-BKGD	197.9	17.4	1639	14	7.8 ± 4.0	1030.63 ± 0.10	90 ± 110	-387 ± 30	0.051	1680 ± 50	397 ± 3
S40507	HD96548-BKG	292.3	-4.8	13133	8	2.9 ± 1.2	1031.65 ± 0.03	1 ± 350	-90 ± 10	0.810	303 ± 24	...

TABLE 3 — *Continued*

Sight Line	Target Name ^a	l (deg)	b (deg)	t^b (s)	Bin ^c	Intensity ^d (10^3 LU)	Wavelength ^e (Å)	FWHM ^f (km s ⁻¹)	v_{LSR} (km s ⁻¹)	$E(B - V)^g$ (mag)	SXR ^h (RU)	H α ⁱ (10^3 LU)
S40510	NCVZ-BKGD	117.2	46.3	40524	8	1.0 \pm 0.5	1030.46 \pm 0.04	5 \pm 50	-415 \pm 13	0.012	1140 \pm 30	9 \pm 4
S40513	PG1032+406-BKGD	178.9	59.0	12206	14	2.9 \pm 1.9	1031.79 \pm 0.11	120 \pm 170	-39 \pm 32	0.013	1500 \pm 50	51
S40514	HD163522-BKGD	349.6	-9.1	21826	8	6.3 \pm 2.8	1032.27 \pm 0.29	410 \pm 190	104 \pm 85	0.182	260 \pm 60	...
S40529	HD013268-BKGD	134.0	-5.0	11803	8	2.1 \pm 1.1	1031.42 \pm 0.10	60 \pm 30	-142 \pm 29	0.411	373 \pm 23	443 \pm 3
S40534	EG50-BKGD	178.3	15.4	2204	14	9.5 \pm 3.7	1031.53 \pm 0.06	40 \pm 120	-122 \pm 18	0.129	400 \pm 30	102 \pm 3
S40537	RE0503-289-BKGD	230.7	-34.9	20940	8	2.7 \pm 1.1	1032.04 \pm 0.11	60 \pm 90	13 \pm 33	0.015	1220 \pm 40	249 \pm 4
S40541	SWUMa-BKGD	164.8	37.0	2285	14	9.2 \pm 4.9	1032.05 \pm 0.30	300 \pm 160	36 \pm 87	0.037	610 \pm 50	54
S40552	NCVZ-BKGD	105.3	54.3	2063	14	6.8 \pm 5.7	1030.78 \pm 0.13	70 \pm 200	-319 \pm 38	0.012	1310 \pm 40	24 \pm 2
S40555	PG1520+525-BKGD	85.4	52.3	31588	8	2.1 \pm 1.0	1031.26 \pm 0.08	80 \pm 100	-177 \pm 22	0.015	1240 \pm 30	35
S40568	V3885-Sgr-BKGD	357.5	-27.8	11873	8	4.6 \pm 1.8	1031.91 \pm 0.08	100 \pm 80	0 \pm 22	0.062	690 \pm 50	...
S40581	HD113001-BKGD	110.3	81.7	14244	14	3.6 \pm 1.4	1031.79 \pm 0.14	200 \pm 40	-29 \pm 42	0.010	1090 \pm 30	26 \pm 3
S40594	HD219188-BKGD	83.0	-50.2	9218	14	3.2 \pm 1.6	1034.03 \pm 0.12	100 \pm 60	614 \pm 36	0.072	440 \pm 30	51 \pm 3
S50505	NEAR-WD2211-495-BKGD	345.6	-52.2	11026	14	2.7 \pm 1.3	1031.92 \pm 0.11	110 \pm 90	-4 \pm 33	0.016	1010 \pm 40	...
S50515	MRK876-BKGD	90.5	56.6	5832	8	2.9 \pm 1.4	1032.75 \pm 0.03	3 \pm 20	255 \pm 7	0.016	1080 \pm 30	62 \pm 3
S50523	EC11481-2303-BKGD	285.3	37.4	5042	14	5.6 \pm 3.3	1031.60 \pm 0.40	300 \pm 40	-99 \pm 117	0.056	660 \pm 30	112 \pm 3
S50529	PG0242+132-BKGD	160.6	-41.0	3572	14	4.9 \pm 2.0	1030.41 \pm 0.07	5 \pm 70	-448 \pm 20	0.104	510 \pm 40	83 \pm 3
S50540	BD+523210-BKGD	102.4	-3.4	10035	8	2.6 \pm 1.2	1031.18 \pm 0.03	3 \pm 20	-203 \pm 8	0.460	317 \pm 23	1450 \pm 4
S50542	PG0919+272-BKGD	200.5	43.9	5307	14	5.8 \pm 2.5	1032.03 \pm 0.12	160 \pm 100	23 \pm 36	0.023	690 \pm 30	59 \pm 3
S51601	HD104994-BKGD	297.6	0.3	17129	8	7.9 \pm 3.4	1032.04 \pm 0.26	410 \pm 150	25 \pm 75	3.504	350 \pm 40	...
Z90711	RXJ1729.1+7033	101.3	32.3	21722	8	1.6 \pm 0.6	1031.74 \pm 0.04	5 \pm 100	-39 \pm 13	0.034	691 \pm 13	83 \pm 3
Z90726	IRAS05595-5756	266.5	-29.4	21079	14	2.0 \pm 0.8	1032.10 \pm 0.09	100 \pm 30	32 \pm 27	0.045	511 \pm 17	...
Z90733	NGC3735	131.7	45.3	6967	14	3.5 \pm 1.4	1031.41 \pm 0.06	20 \pm 90	-140 \pm 18	0.017	1030 \pm 30	24 \pm 3

^a Target names are taken from the data file headers. Some have been modified for this table.^b Exposure time is night only.^c Spectral binning in 0.013 Å pixels.^d 1 LU = 1 photon s⁻¹ cm⁻² sr⁻¹.^e Wavelengths are heliocentric.^f Gaussian FWHM values include the smoothing imparted by the instrument optics. Values less than ~ 25 km s⁻¹ indicate that the emission does not fill the LWRS aperture.^g Extinction from Schlegel et al. 1998.^h *ROSAT* 1/4 keV emission from Snowden et al. 1997. 1 RU = 10^{-6} counts s⁻¹ arcmin⁻².ⁱ H α intensity integrated over the velocity range -80 to +80 km s⁻¹ from Haffner et al. 2003. Values without error bars were derived from the average of the surrounding pointings. Data are available only for declinations above -30°.

TABLE 4
O VI $\lambda 1032$ 3σ UPPER LIMITS

Sight Line	Target Name ^a	l (deg)	b (deg)	l^b (s)	3σ Limit ^c (10^3 LU)	$E(B - V)^d$ (mag)	SXR ^e (RU)	H_α^f (10^3 LU)
A01002	LB9802	299.9	-30.7	2022	5.8	0.077	630 \pm 40	...
A03406	WD2218+706	110.9	11.5	1582	5.9	0.689	470 \pm 30	699 \pm 4
A03407	RE-J0558-376	243.7	-26.1	8143	3.1	0.036	770 \pm 30	...
A04802	HH47A	267.4	-7.5	6297	3.9	1.095	570 \pm 24	...
A05101	HD200775	104.1	14.2	14786	2.0	12.290	364 \pm 19	361 \pm 4
A11701	ComaI	57.6	88.0	23614	1.5	0.009	4370 \pm 90	...
A13902	NGC1068	172.1	-51.9	77189	0.9	0.034	610 \pm 50	64 \pm 3
B01805	NGC5471	101.8	59.6	6303	3.5	0.010	1320 \pm 40	35 \pm 3
B04604	HD206267C	99.3	3.7	10072	2.6	0.963	283 \pm 17	14237
B06801	GAMMA-CRU	300.2	5.6	12104	3.0	0.789	390 \pm 30	...
C02201	HD6833	125.6	-8.0	17498	2.2	0.444	440 \pm 50	602 \pm 4
C02301	BETA-GRU	346.3	-58.0	5677	3.0	0.009	1170 \pm 50	...
C03701	PG1626+554	84.5	42.2	29854	1.4	0.006	1430 \pm 30	38
C03702	NGC7714	88.2	-55.6	77143	0.9	0.052	430 \pm 30	47
C11602	CD-38-10980	341.5	7.3	5939	4.0	0.885	1350 \pm 50	...
C11603	HD74389B	170.6	38.6	29341	1.6	0.030	1120 \pm 50	56 \pm 3
D05801	WD2013+400	77.0	3.2	30059	1.8	2.524	468 \pm 20	13413 \pm 12
D11701	3C249.1	130.4	38.5	39169	1.4	0.032	770 \pm 40	61 \pm 4
D12003	IC4593	25.3	40.8	5297	4.8	0.058	700 \pm 30	231 \pm 3
D12017	PK342-14D1	342.5	-14.3	3539	4.7	0.131	580 \pm 110	...
D15801	WD2020-425	358.4	-34.5	11638	2.3	0.054	880 \pm 50	...
D90301	SBS1116+518	152.0	60.1	22775	1.7	0.014	1090 \pm 50	34 \pm 3
D90302	IRAS03335-5626	269.4	-48.9	33946	1.5	0.025	840 \pm 30	...
M10103	GD71	192.0	-5.3	9411	2.6	0.300	390 \pm 30	662 \pm 3
M10704	WD0439+466	158.5	0.5	43550	1.7	1.139	310 \pm 30	1359 \pm 4
P10409	HD029139	181.0	-20.2	11882	2.2	0.592	430 \pm 40	813
P10421	WD1202+608	133.1	55.7	50097	1.2	0.015	920 \pm 40	19 \pm 2
P10425	HD128620/HD128621	315.7	-0.7	26651	1.6	6.505	340 \pm 30	...
P11607	HD38087	207.1	-16.3	2041	11.2	0.717	421 \pm 23	5960 \pm 7
P12012	JUP-DTOH2	194.3	13.3	4899	3.7	0.054	1070 \pm 40	352 \pm 3
P19802	NGC7293	36.2	-57.1	4394	6.4	0.318	710 \pm 40	2163 \pm 5
P20406	WD2127-222	27.4	-43.8	18938	2.0	0.046	700 \pm 40	75
P20419	WD1615-154	358.8	24.2	13891	2.5	0.305	690 \pm 100	812 \pm 4
P20421	WD0715-704	281.6	-23.5	4489	4.6	0.222	660 \pm 30	...
P30208	LB1566	306.4	-62.0	8022	3.7	0.019	760 \pm 60	...
Q10803	PK010-081	9.9	-7.6	3989	3.5	0.326	280 \pm 30	895
S10102	WD1634-573	329.9	-7.0	67118	1.2	0.342	450 \pm 40	...
S40501	PG0749+658-BKGD	150.5	31.0	21619	1.5	0.045	530 \pm 30	69 \pm 3
S40512	HD163892	7.2	0.6	4259	4.2	7.781	320 \pm 40	2583 \pm 5
S40515	HD92809-BKGD	286.8	-0.0	14880	2.5	1.921	380 \pm 30	...
S40518	WD2111+498-BKGD	91.4	1.1	19746	1.9	2.804	445 \pm 23	1552 \pm 4
S40521	BD+28D4211-BKGD	81.9	-19.3	13312	2.3	0.094	370 \pm 30	456
S40522	HD216438-BKGD	105.7	-5.1	3945	3.7	0.399	280 \pm 30	897 \pm 4
S40523	WOLF1346-BKGD	67.2	-9.0	9653	2.5	0.214	449 \pm 22	413 \pm 4
S40524	HD203374A-BKGD	100.5	8.6	41564	1.2	1.052	312 \pm 16	2574 \pm 6
S40525	A43-BKGD	36.1	17.6	2824	4.6	0.192	440 \pm 30	225 \pm 3
S40526	HD156385-BKGD	343.2	-4.8	7063	3.1	0.530	320 \pm 30	...
S40528	HD187459-BKGD	68.8	3.9	12190	2.3	0.677	390 \pm 25	3148
S40531	GD50-BKGD	189.0	-40.1	5867	3.3	0.186	720 \pm 30	1402 \pm 4
S40532	BD+532820-BKGD	101.2	-1.7	20938	1.8	0.544	240 \pm 17	1518 \pm 5
S40533	WZSge-BKGD	57.5	-7.9	7651	3.6	0.315	560 \pm 30	424 \pm 4
S40535	HD1383-BKGD	119.0	-0.9	3684	3.9	1.539	410 \pm 40	2331
S40540	PG0952+519-BKGD	164.1	49.0	14690	2.0	0.010	1010 \pm 40	66 \pm 4
S40542	Abell78-BKGD	81.3	-14.9	5480	3.6	0.164	280 \pm 30	389 \pm 4
S40550	Z-Cam-BKGD	141.4	32.6	14894	2.0	0.027	590 \pm 30	73 \pm 3
S40553	WR42-HD97152-BKGD	290.9	-0.5	11844	2.9	1.571	300 \pm 30	...
S40558	HD102567-BKGD	295.6	-0.2	7400	3.5	3.790	420 \pm 30	...
S40559	BD+354258-BKGD	77.2	-4.7	7758	3.6	0.583	499 \pm 25	2643
S40561	CVZ-BKGD	99.3	43.3	5666	3.2	0.034	490 \pm 30	42 \pm 3
S40562	NGC4194-BKGD	134.4	61.8	14414	1.9	0.016	860 \pm 40	38 \pm 2
S40564	BD+43D4035-BKGD	100.6	-13.1	5020	3.3	0.263	230 \pm 16	320
S40565	HD182308-BKGD	95.5	21.3	3630	4.0	0.103	416 \pm 15	235 \pm 3
S40566	HD192035-BKGD	83.3	7.8	32619	1.4	0.439	485 \pm 18	1794 \pm 5
S40570	BD+48658-BKGD	138.1	-11.1	23293	1.8	0.163	520 \pm 30	410 \pm 3
S40572	HD21291-BKGD	141.5	2.9	13773	2.2	1.317	290 \pm 22	1285
S40573	HD35580-BKGD	264.2	-34.5	40611	1.3	0.040	620 \pm 40	...
S40574	PG1051+501-BKGD	159.9	58.5	7500	2.8	0.019	930 \pm 30	40 \pm 3
S40577	HDE232522-BKGD	130.7	-6.7	5295	3.6	0.278	430 \pm 40	792 \pm 4
S40582	CD-61_1208-BKGD	270.1	-30.6	42039	1.2	0.052	452 \pm 15	...
S40583	WD1234+481-BKGD	129.8	69.0	3842	4.3	0.016	1160 \pm 50	41 \pm 2
S40587	BKGD_1_mps413	161.9	64.7	8104	2.5	0.014	1220 \pm 40	27 \pm 3
S40588	BKGD_2_mps413	150.6	58.9	12295	2.2	0.017	1100 \pm 50	16 \pm 3
S40589	JL25-BKGD	318.6	-29.2	9891	2.6	0.116	470 \pm 60	...
S50502	G191-B2B-BKGD	156.0	7.1	56693	1.1	0.615	300 \pm 30	213 \pm 3
S50506	HD201345-BKGD	78.4	-9.5	4867	4.9	0.191	398 \pm 22	1040 \pm 4
S50507	HD71634-BKGD	273.3	-11.5	10265	2.8	0.261	400 \pm 30	...
S50512	NGC1360-BKGD	220.0	-54.4	8256	2.9	0.011	2100 \pm 500	336 \pm 3
S50514	HD5679-BKGD	123.3	19.0	10122	2.6	0.246	440 \pm 30	136 \pm 3

TABLE 4 — *Continued*

Sight Line	Target Name ^a	l (deg)	b (deg)	t^b (s)	3σ Limit ^c (10^3 LU)	$E(B - V)^d$ (mag)	SXR ^e (RU)	H α ^f (10^3 LU)
S50516	HD46223-BKGD	206.4	-2.1	13659	2.2	1.306	520 \pm 30	3601
S50517	HD37367-BKGD	179.0	-1.0	9830	2.3	1.472	334 \pm 24	978
S50518	UV0904-02-BKGD	233.0	28.1	12085	2.7	0.020	820 \pm 40	80 \pm 3
S50522	HD190864-BKGD	72.5	2.0	6213	3.5	2.175	397 \pm 22	10786
S50525	PG1519+640-BKGD	100.3	46.2	7467	3.4	0.016	1120 \pm 30	28 \pm 3
S50527	Feige108-BKGD	76.8	-55.9	4424	3.2	0.044	500 \pm 40	52 \pm 3
S50530	DeHt2-BKGD	27.7	16.9	2377	6.4	0.251	350 \pm 30	249 \pm 3
S50533	HD29094-BKGD	161.8	-4.0	7436	2.3	0.511	273 \pm 23	216
S50536	HD36408-BKGD	188.5	-8.9	17691	1.7	0.579	306 \pm 22	1124
S50538	HD060369-BKGD	242.7	-4.3	4838	4.1	0.513	700 \pm 40	2786 \pm 5
S50539	GD1618-BKGD	16.2	-76.7	3148	3.8	0.020	760 \pm 40	59 \pm 4
S50543	PG0101+039-BKGD	128.9	-58.5	4095	3.0	0.021	520 \pm 40	54 \pm 3
S51303	HD092702	286.1	1.0	3434	5.6	1.182	380 \pm 30	...
S51401	CPD-721184	299.2	-10.9	5955	4.0	0.241	220 \pm 30	...
S52001	HD186994	78.6	10.1	2271	7.9	0.201	337 \pm 19	1683
S52301	WD2211-495-BKGD	345.8	-52.6	58547	1.2	0.015	960 \pm 40	...
S52307	AGK+81D266-BKGD	130.7	31.9	17424	2.5	0.026	780 \pm 30	108
S52309	HD179406	28.2	-8.3	5487	3.1	0.499	230 \pm 24	397
Z90702	CTS0563	354.7	-49.9	15329	1.5	0.017	990 \pm 50	...
Z90706	MRK474	87.0	60.6	5759	3.3	0.033	770 \pm 30	55
Z90708	HE2336-5540	322.8	-58.9	12485	3.0	0.011	1280 \pm 60	...
Z90709	PG1246+586	123.7	58.8	8016	3.1	0.011	1150 \pm 40	30 \pm 2
Z90712	FB1229+710	125.3	46.3	5509	3.5	0.018	1000 \pm 30	60 \pm 3
Z90714	87GB163624.4+713451	103.9	36.2	11021	1.9	0.045	554 \pm 14	88 \pm 3
Z90719	ESO116-G18	276.2	-47.6	10485	2.0	0.075	780 \pm 40	...
Z90721	PKS0355-483	256.2	-48.5	11866	2.5	0.006	990 \pm 50	...
Z90722	NGC1566	264.3	-43.4	2425	4.4	0.009	810 \pm 40	...
Z90725	ESO253-G03	252.0	-33.7	12401	2.5	0.043	710 \pm 30	...
Z90727	UGC3478	151.4	22.1	2988	3.7	0.092	440 \pm 30	114 \pm 3
Z90735	MRK486	86.9	49.4	18011	2.0	0.014	1170 \pm 30	42
Z90736	NGC6521	91.8	30.2	27742	1.3	0.041	722 \pm 10	61 \pm 3
Z90737	FAIRALL333	327.7	-23.8	29366	1.4	0.083	450 \pm 70	...

^a Target names are taken from the data file headers.^b Exposure time is night only.^c 1 LU = 1 photon s⁻¹ cm⁻² sr⁻¹.^d Extinction from Schlegel et al. 1998.^e ROSAT 1/4 keV emission from Snowden et al. 1997. 1 RU = 10⁻⁶ counts s⁻¹ arcmin⁻².^f H α intensity integrated over the velocity range -80 to +80 km s⁻¹ from Haffner et al. 2003. Values without error bars were derived from the average of the surrounding pointings. Data are available only for declinations above -30°.TABLE 5
O VI TOWARD NEARBY WHITE DWARFS

Sight Line	White Dwarf	d (pc)	Absorption			Emission
			v_{Helio} (km s ⁻¹)	b (km s ⁻¹)	$\log N$ (cm ⁻²)	v_{Helio} (km s ⁻¹)
P20411	WD 0004+330	97	-3.8 \pm 3.6	21.3 \pm 4.1	12.79 \pm 0.09	-6 \pm 15
P10411	WD 0455-282	102	-23.6 \pm 4.6	30.1 \pm 7.4	13.42 \pm 0.07	7 \pm 9
P10429	WD 1631+781	67	-16.4 \pm 5.1	...	12.52 \pm $^{0.12}_{0.17}$	-64 \pm 40
P20422	WD 2004-605	58	-23.2 \pm 6.4	...	13.00 \pm 0.10	-6 \pm 8

NOTE. — Stellar distances and absorption data are from Savage & Lehner 2006, who use the interstellar C II λ 1036.34 line to tie their velocity scale to that of Holberg et al. 1998. Emission-line velocities are from this paper.TABLE 6
OBSERVATIONS INCLUDED IN SIGHT LINE B12901

Observation ID	l^a (deg)	b^a (deg)	t^b (s)	Intensity ^c (10^3 LU)	Wavelength ^d (Å)	FWHM (km s ⁻¹)	v_{LSR} (km s ⁻¹)
I2050501, I2050510	278.58	-45.31	46386	3.0 \pm 0.6	1032.69 \pm 0.05	100 \pm 20	206 \pm 13
I2050601	278.59	-45.30	11120	< 2.2
B1290101, B1290102	278.63	-45.31	26073	< 1.5

^a Coordinates of LWRS aperture from Shelton 2003.^b Exposure time is night only.^c 1 LU = 1 photon s⁻¹ cm⁻² sr⁻¹.^d Wavelength is heliocentric.

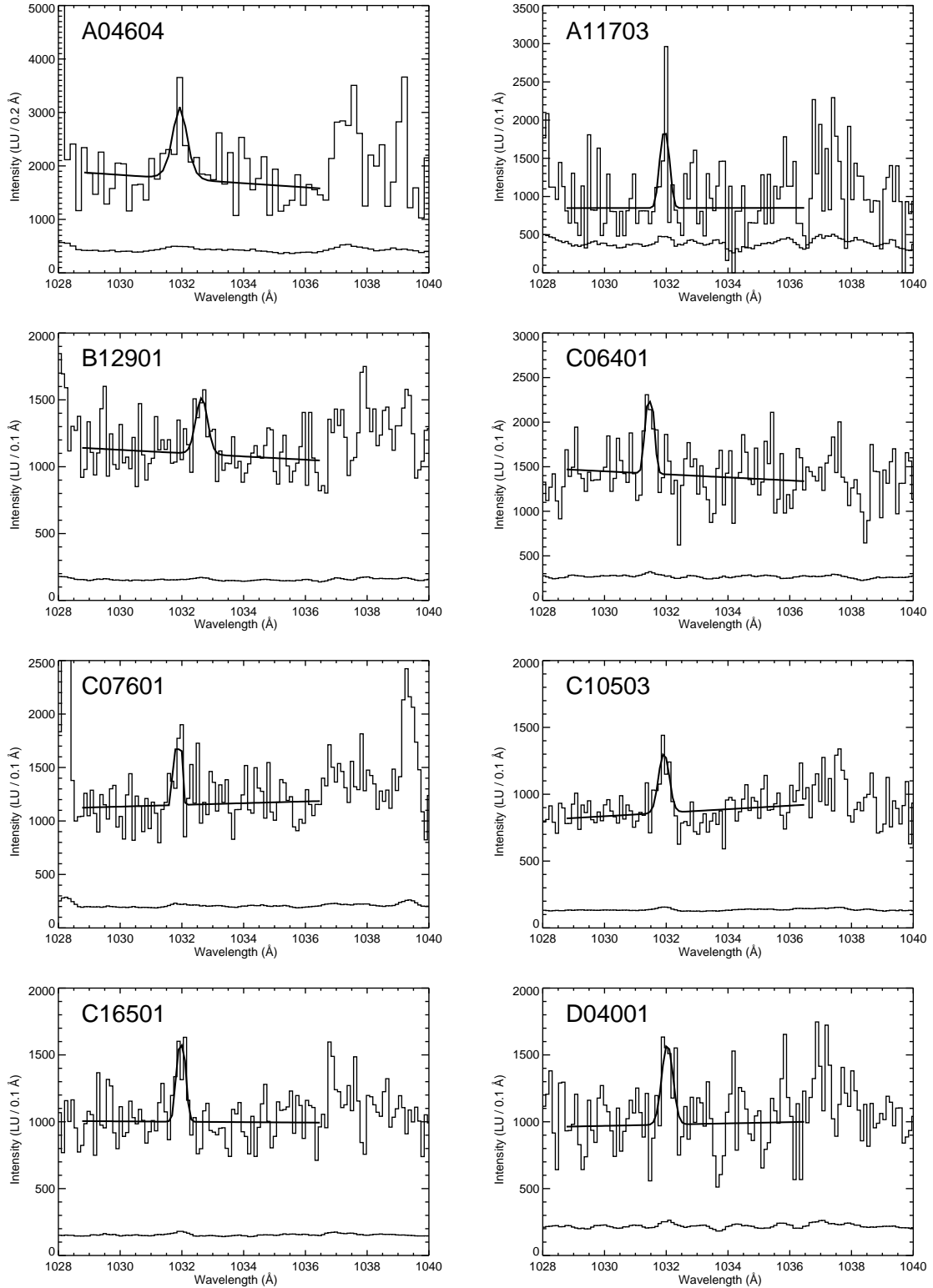
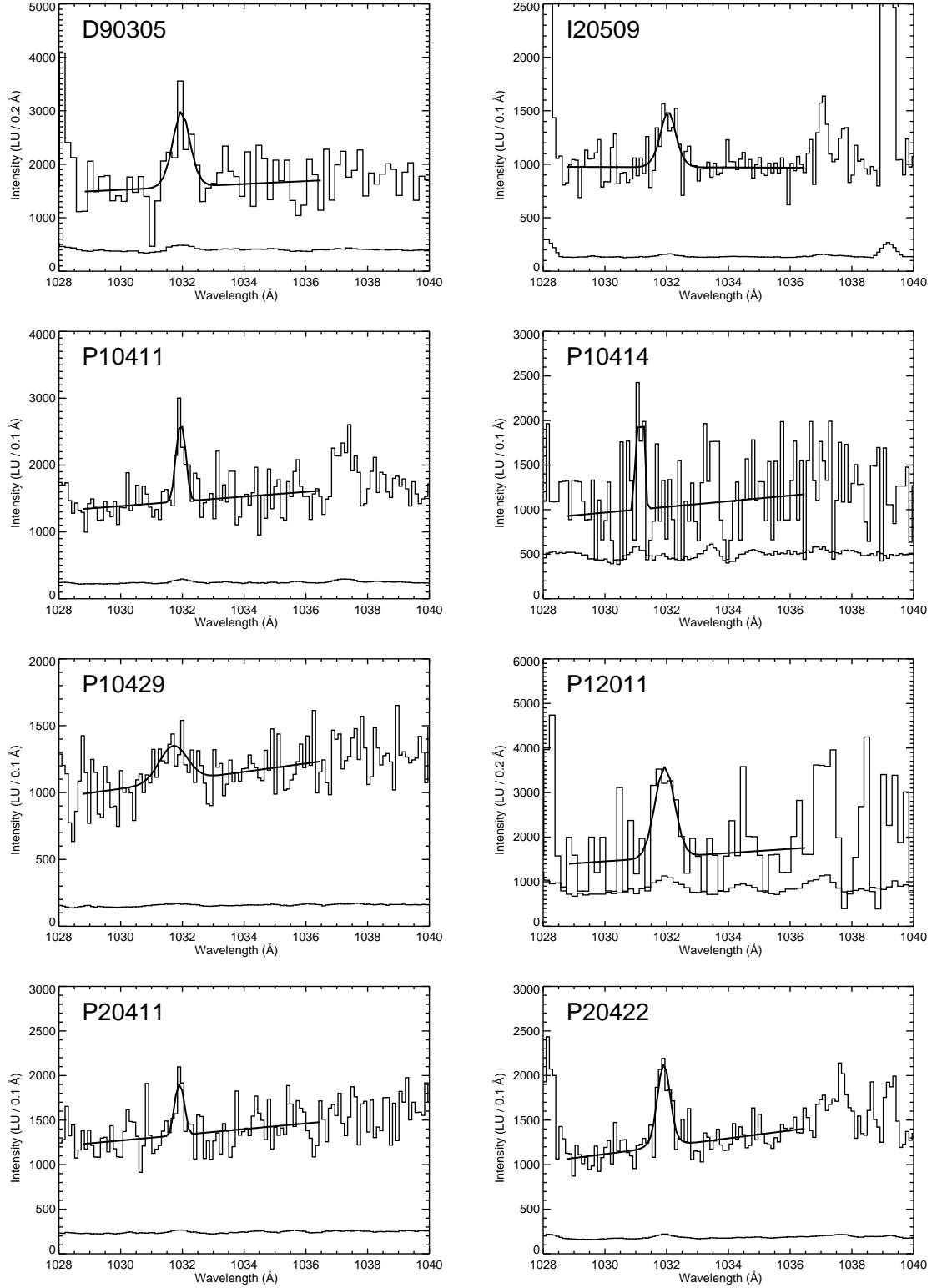


FIG. 2.— High-significance (3σ) O VI $\lambda 1032$ emission features. The data are binned by the factors given in Table 3, and best-fit model spectra and error bars are overplotted. Interstellar C II* $\lambda 1037$ and O VI $\lambda 1038$ are present in some spectra, as are the geocoronal O I $\lambda\lambda 1028, 1039$ lines.

*Fig. 2. — Continued.*

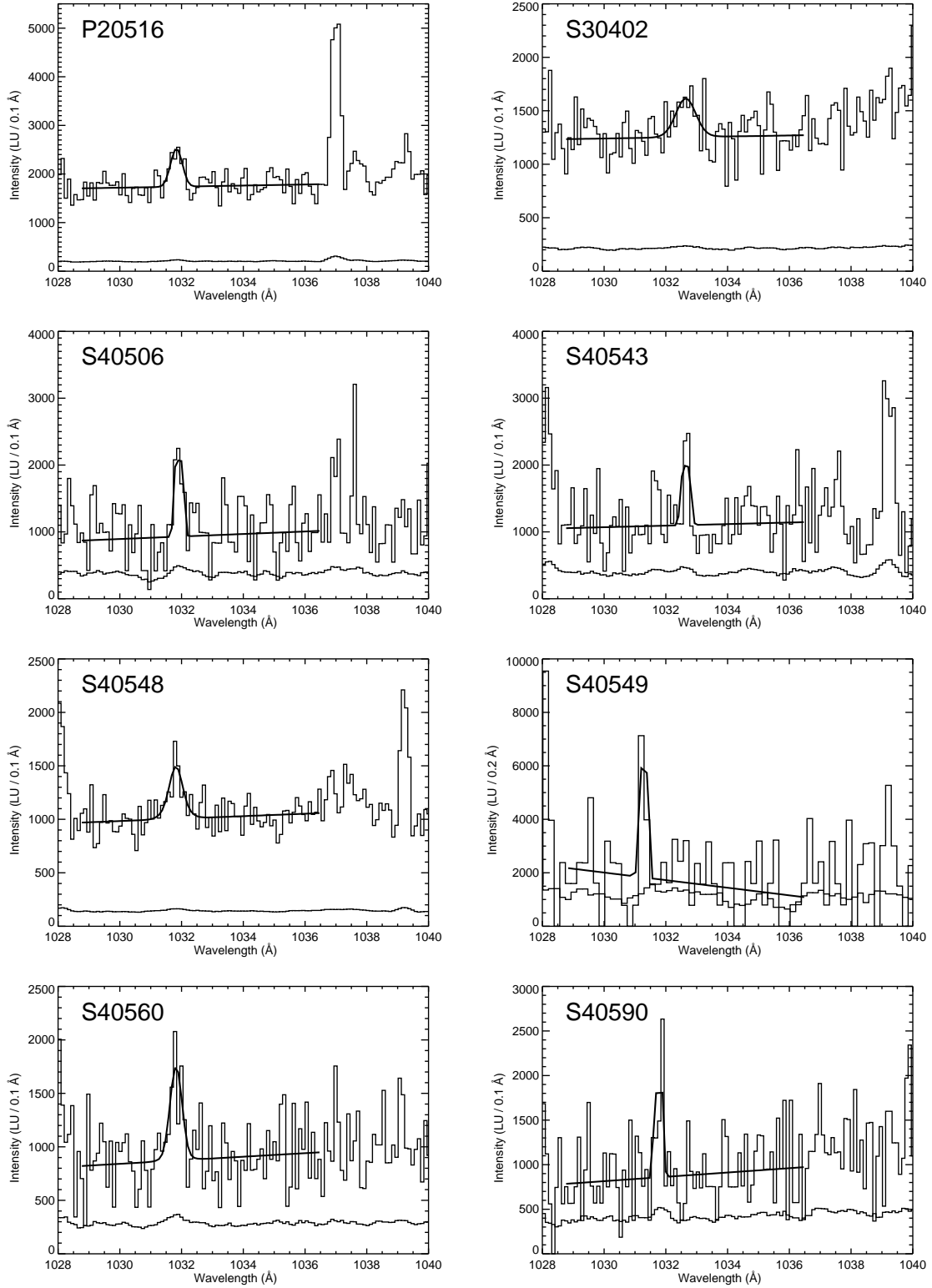


Fig. 2. — Continued.

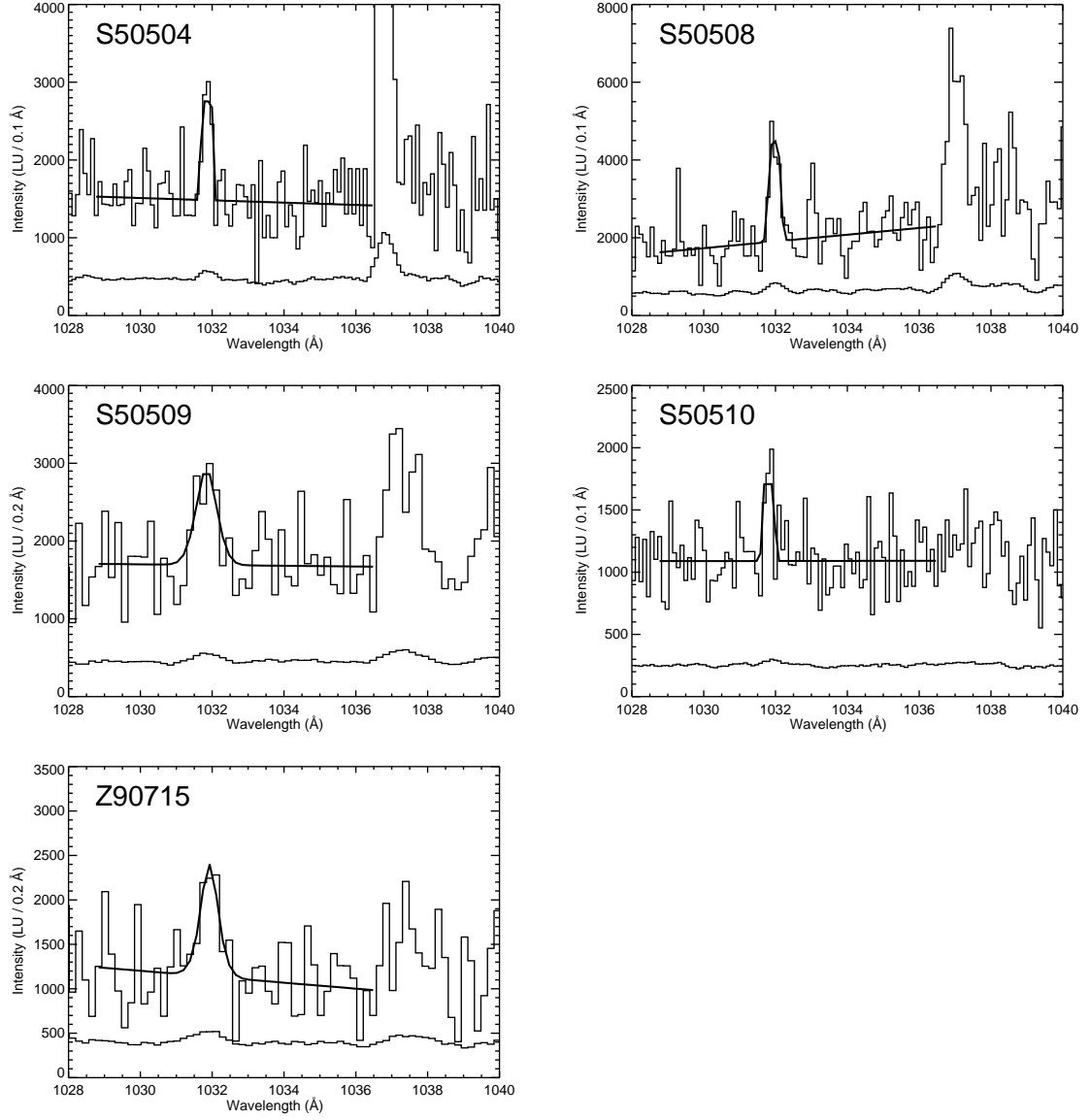


Fig. 2. — Continued.

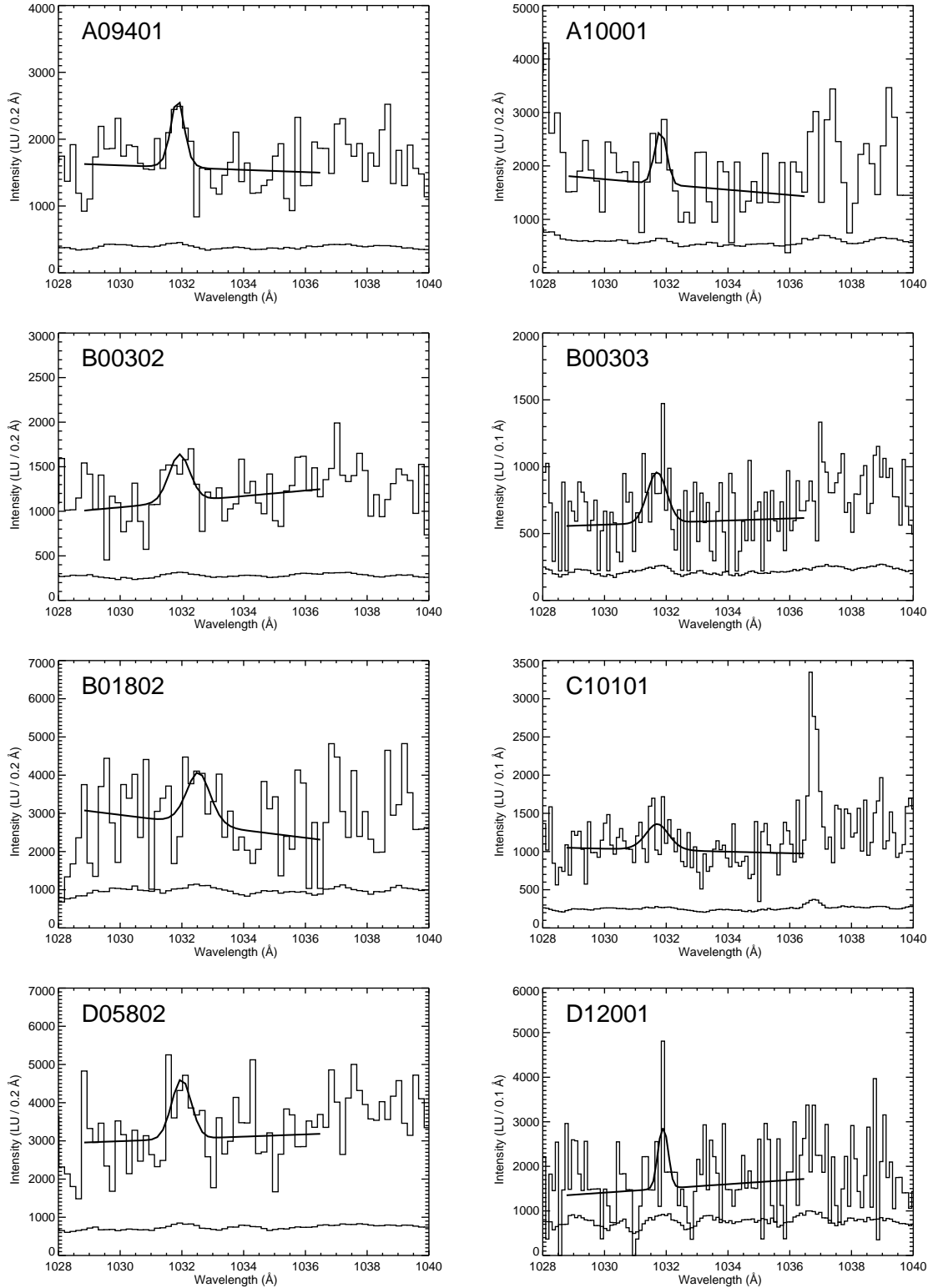
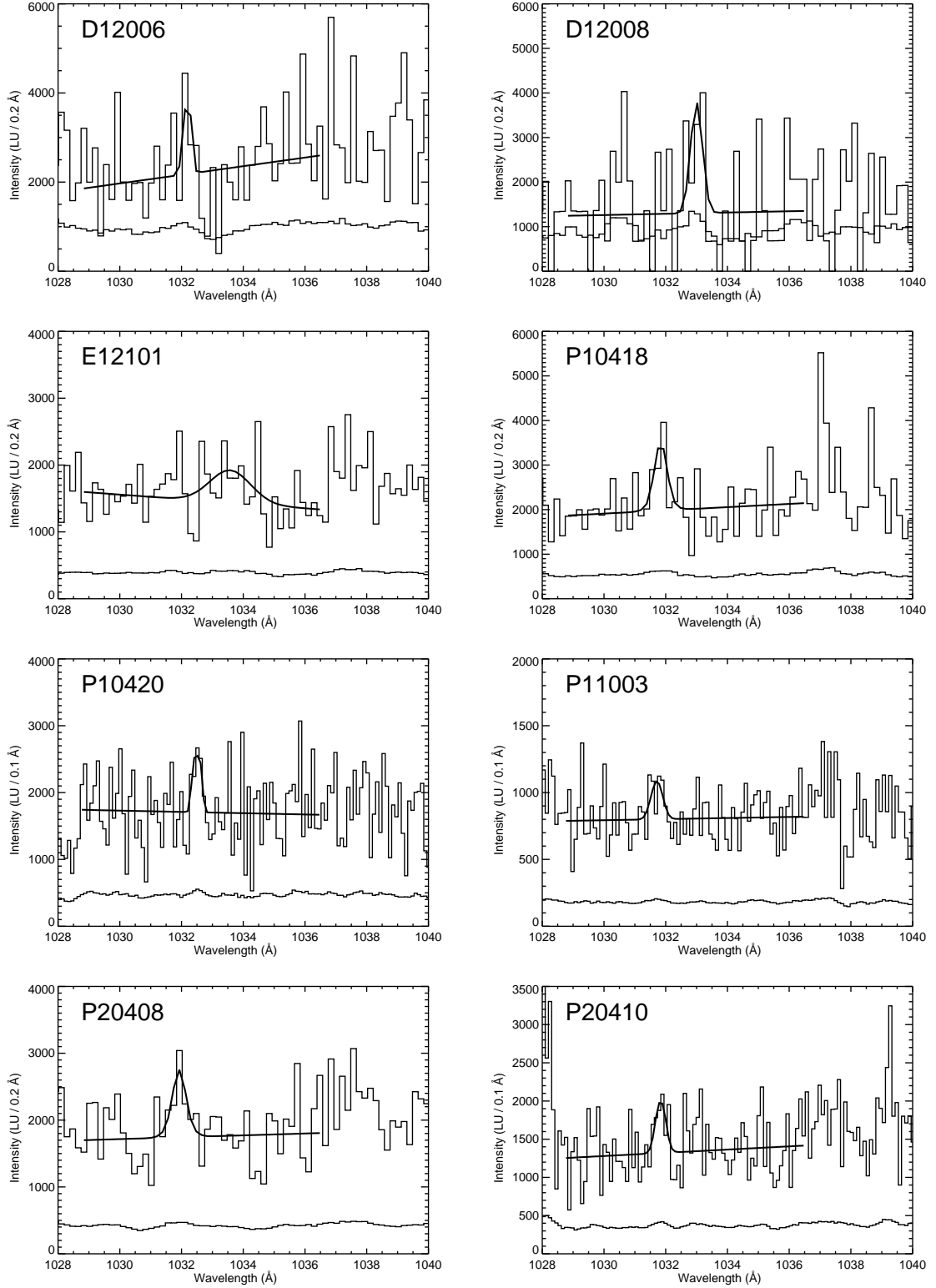


FIG. 3.— Low-significance (2σ) O VI $\lambda 1032$ emission features. The data are binned by the factors given in Table 3, and best-fit model spectra and error bars are overplotted. Interstellar C II* $\lambda 1037$ and O VI $\lambda 1038$ are present in some spectra, as are the geocoronal O I $\lambda\lambda 1028, 1039$ lines.

Fig. 3. — *Continued.*

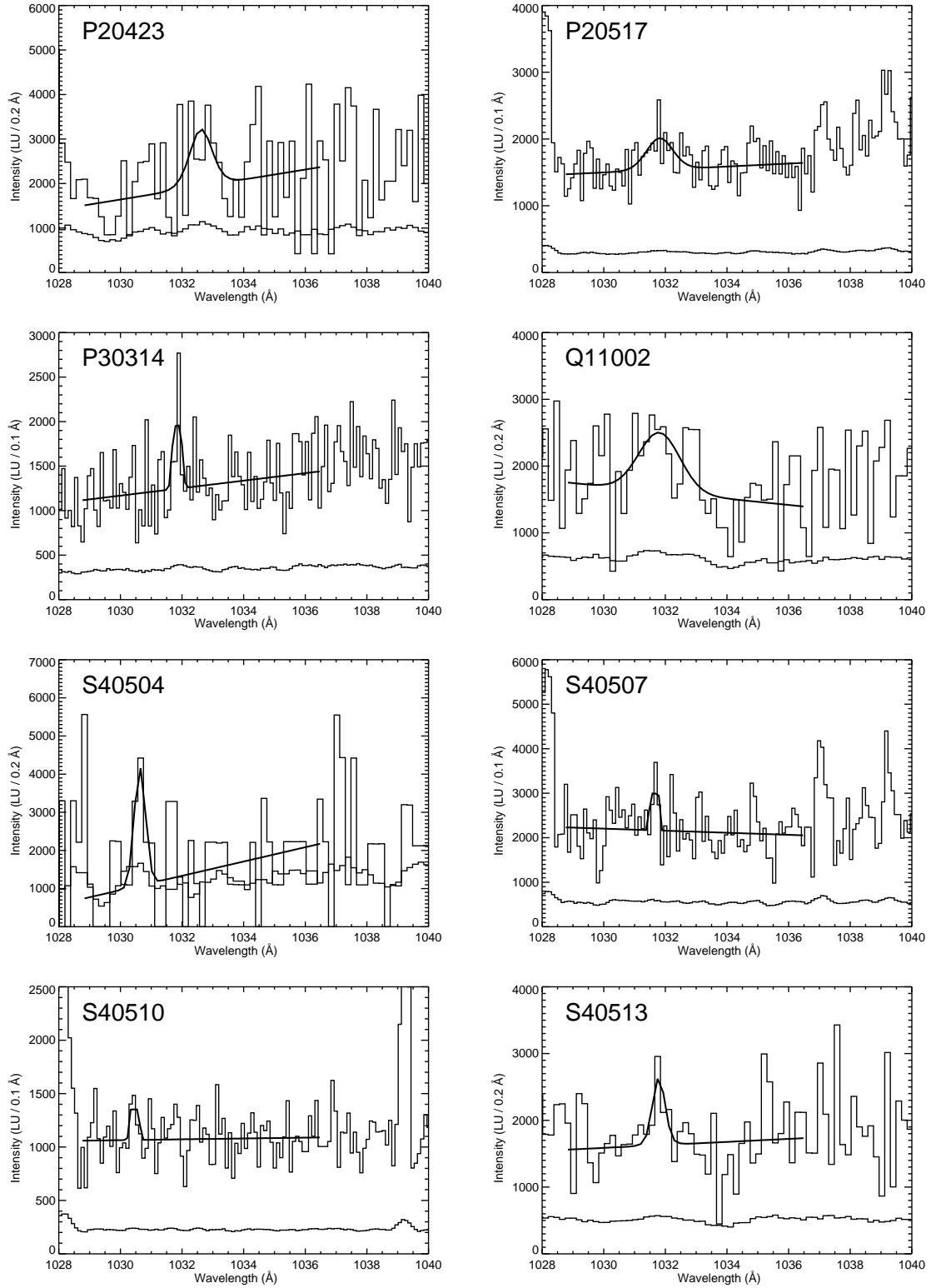
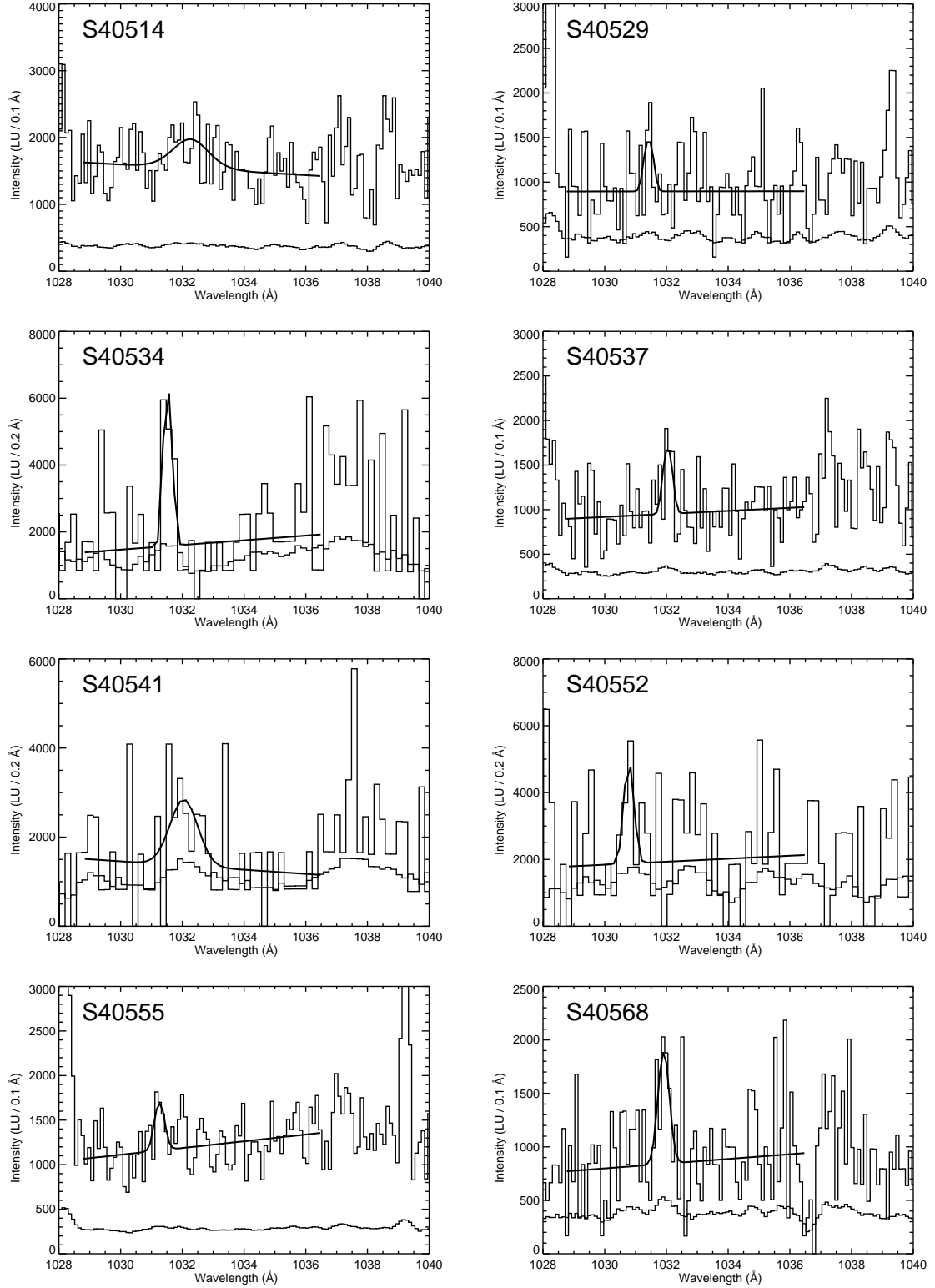


Fig. 3. — Continued.

Fig. 3. — *Continued.*

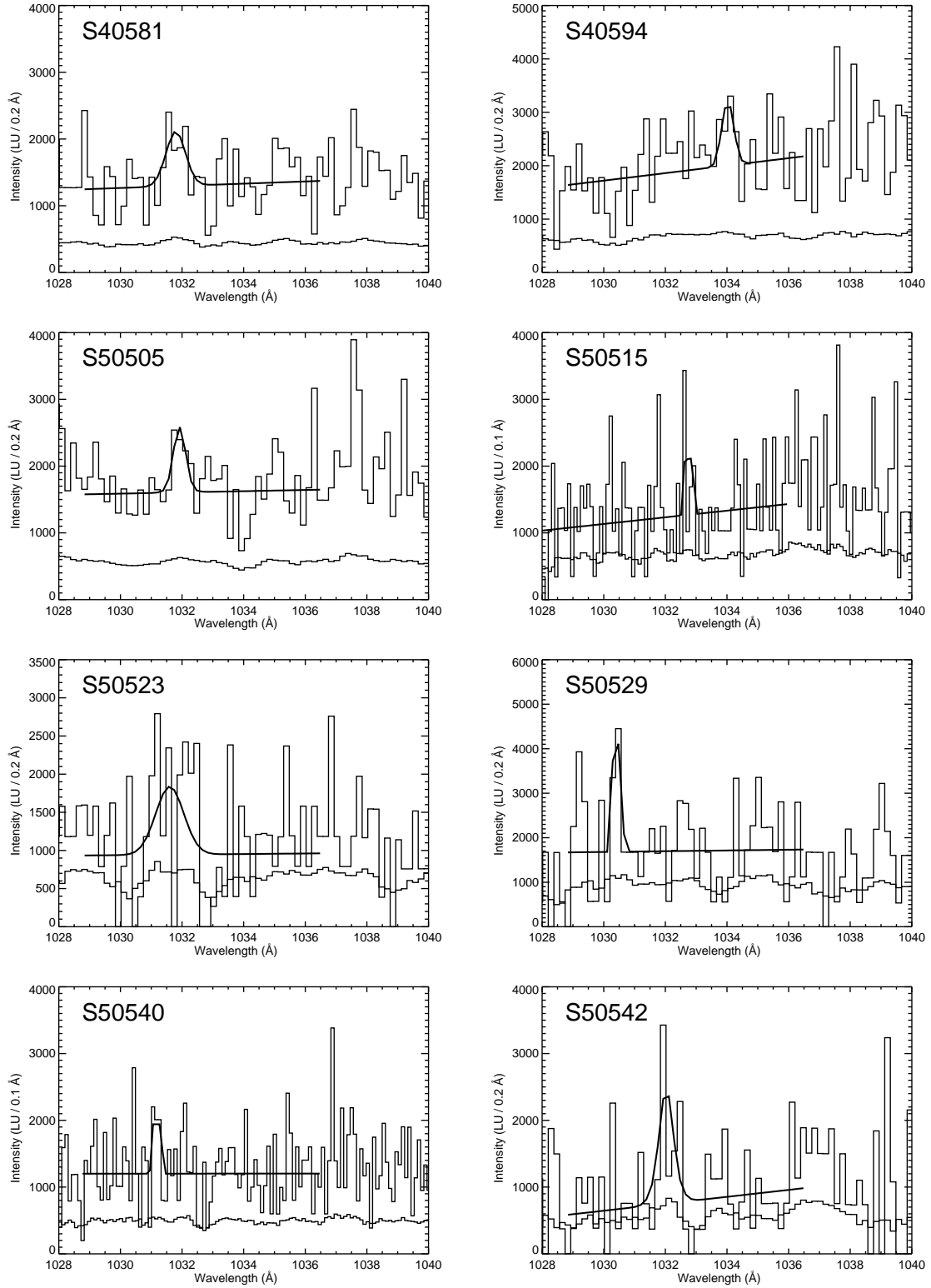


Fig. 3. — Continued.

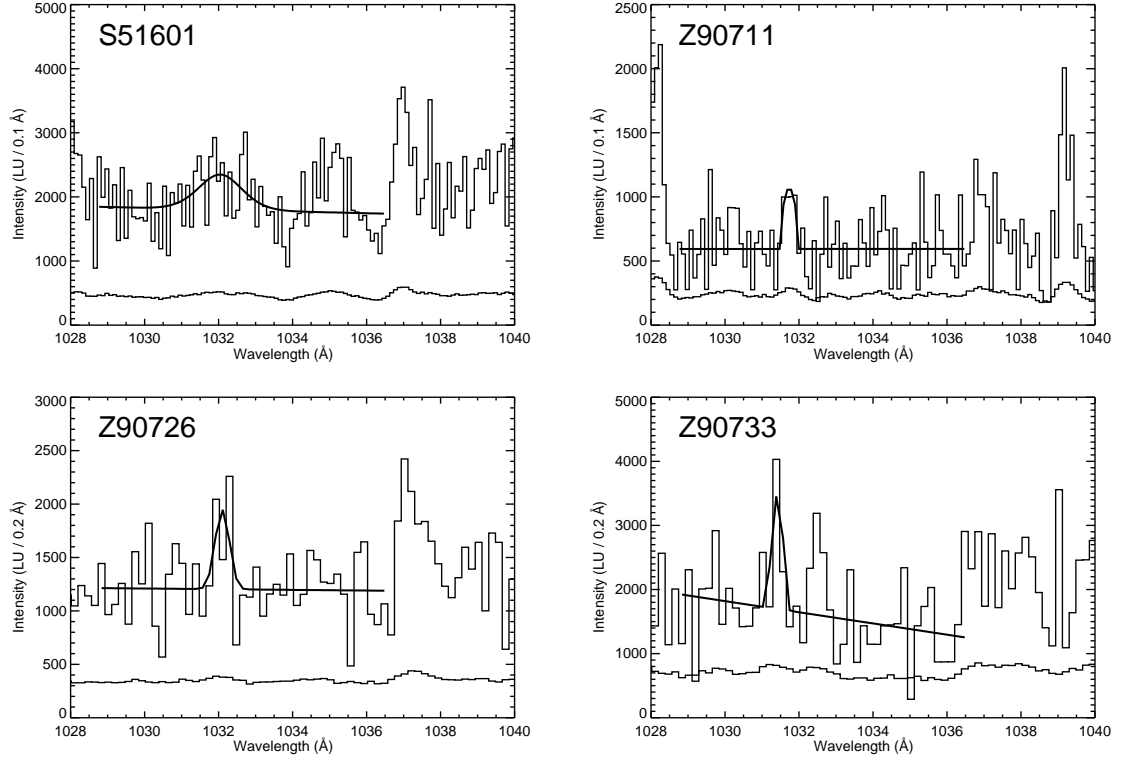


Fig. 3. — Continued.